RMetS
Royal Meteorological Society

Multi-sensor observations of a wave beneath an impacting rear-inflow jet in an elevated mesoscale convective system

J. H. Marsham,[a]* K. A. Browning,[b] J. C. Nicol,[c] D. J. Parker,[b] E. G. Norton,[d] A. M. Blyth,[a] U. Corsmeier[e] and F. M. Perry[a]

[a]*National Centre for Atmospheric Science (NCAS), University of Leeds, UK*
[b]*University of Leeds, UK*
[c]*NCAS, Facility for Ground-based Atmospheric Measurements (FGAM), University of Reading, UK*
[d]*NCAS, University of Manchester, UK*
[e]*Karlsruhe Institute of Technology, Germany*
*Correspondence to: J. H. Marsham, School of Earth and Environment, University of Leeds, Leeds, LS2 9JT, UK.
E-mail: jmarsham@env.leeds.ac.uk

Observations of a wave generated below, and propagating with, an elevated mesoscale convective system (MCS) are presented. The MCS and the wave tracked directly across the 90 km extent of the observational network deployed for the Convective Storm Initiation Project (CSIP) and maintained a coherent structure and velocity during this 1.5 hour period. The rear-inflow jet of the MCS was observed to impact upon, but not penetrate, the stable undercurrent that was located beneath the MCS, apparently constricting the depth of the undercurrent, which did not participate in the main convective updraught. The wave crest was located approximately 15 km ahead of this constriction. The overall wave led to between 200 and 1000 m of ascent and approximately 1500 m of descent. However, undulations were superimposed on the overall wave, with a wavelength of approximately 7 km and a crest-to-trough amplitude of approximately 1000 m. These undulations were associated with double maxima in surface pressure and the elevation of the observed low-level wind anomaly, where low-level winds were backed by more than 90°. These winds were never at rest relative to the system and the wave was therefore a 'gravity wave without stagnation'. The hydrostatic effect expected from the observed lifting in the wave was broadly consistent with the observed surface pressure perturbation of 2 hPa. No cold-pool outflow was ever observed; instead the observed surface cooling of approximately 4°C was shown to be consistent with reduced solar insolation. The generation of the observed wave structure and its implications for the maintenance of the MCS and numerical modelling of the system are discussed.

Key Words: MCS; gravity wave without stagnation; CSIP (Convective Storm Initiation Project); bore

Received 4 February 2010; Revised 2 June 2010; Accepted 7 June 2010; Published online in Wiley Online Library 13 October 2010

Citation: Marsham JH, Browning KA, Nicol JC, Parker DJ, Norton EG, Blyth AM, Corsmeier U, Perry FM. 2010. Multi-sensor observations of a wave beneath an impacting rear-inflow jet in an elevated mesoscale convective system. *Q. J. R. Meteorol. Soc.* **136**: 1788–1812. DOI:10.1002/qj.669

1. Introduction

A Mesoscale Convective System (MCS) is a weather system that, according to Zipser (1982), exhibits moist convective overturning contiguous with or embedded within a mesoscale circulation that is at least partially driven by the convective processes. In the United Kingdom the convective updraughts in MCSs generally originate from warm air in the boundary layer. However, it has long been realized that this is not necessarily the case when, for example, the MCS forms on the cold side of a front (e.g. Browning and Hill, 1984). This kind of MCS, which does not ingest air from the

planetary boundary layer, is referred to as being 'elevated' (Glickman, 2000).

Studies in the United States have shown that many MCSs do occur on the cold side of a front, so-called Type-1 MCSs (Fritsch and Forbes, 2001), and/or at night when the near-surface air is cold. Colman (1990) went so far as to claim that most cold-season thunderstorms in the United States to the east of the Rocky Mountains, outside of Florida, were likely to be elevated, but some aspects of his method are disputed (Williams, 1991; Colman, 1991). Furthermore, recent simulations of MCSs by Parker (2008) have suggested that a lot of the nocturnal MCSs that would previously have been thought to be elevated may actually be surface based. Nevertheless, there probably does remain a significant proportion of MCSs that are truly elevated. Recent studies during the International H_2O Project (IHOP_2002) indicate that as many as half of the observed 'convective-storm initiation episodes' were elevated (Wilson and Roberts, 2006). Some MCSs may be elevated during only the early or late part of their lifetime (e.g. Marsham *et al.*, 2010), but others remain elevated throughout. Such a storm was observed during Intensive Observing Period (IOP) 3 of the Convective Storm Initiation Project (CSIP), and its structure has been analysed by Browning *et al.* (2010). The focus of that study was on the slantwise updraught and downdraught, the latter constituting a rear-inflow jet (RIJ: Smull and Houze, 1987). The RIJ impacted on, but was unable to penetrate, a cold near-surface layer referred to as an undercurrent, and a complex wave structure was produced within the undercurrent ahead of the RIJ. The purpose of the present paper is to analyse the structure of this wave by synthesizing observations from a variety of ground-based and airborne measurements.

Using a two-dimensional model, Crook and Moncrieff (1988) showed that there can be a continuous evolution of the flow beneath modelled deep convection from a wave to a density current and that modelled convection can be long-lived without a density current forming. Dudhia *et al.* (1987) and Lafore and Moncrieff (1989) both described simulations showing similar results. More recently, again using idealised two-dimensional modelling, Parker (2008) showed that a system with a density current encountering colder low-level air could evolve into a system of elevated convection above a low-level bore-like disturbance, with the system speed increasing as a result.

It is established that even large MCSs can lack downdraughts that penetrate to the surface, leading to an absence of a significant surface density current (Maddox, 1980; Browning and Hill, 1984; Fortune *et al.*, 1992; Smull and Augustine, 1993; Trier and Parsons, 1993). Several researchers (e.g. Dudhia *et al.*, 1987; Schmidt and Cotton, 1990; Buzzi *et al.*, 1991; Parker, 2008; Schumacher and Johnson, 2008; Schumacher, 2009) have simulated systems where the moist convection was located above a low-level wave, rather than a density current, with low-level air ascending and descending in the wave, but with the wave providing uplift required for more elevated air to reach its level of free convection (LFC). However, in all of these studies observational datasets either do not exist or are limited. Since the MCS and wave discussed in the present paper tracked directly across the CSIP observation area, the data presented here are, to the best of the authors' knowledge, the most comprehensive published set of observations of such a low-level wave beneath an MCS.

To set the scene, Figure 1 shows the various features of the MCS that are investigated in this paper. The figure is a vertical section through the lowest 6 km of the storm, along its direction of travel. Figure 1 is qualitatively consistent with vertical sections showing the whole storm depth, up to almost 12 km, that were derived in the companion study of Browning *et al.* (2010); however, it focuses on details of the low-level structure, which are quantified in sections 3 to 7 of the present paper and summarised in section 8 and Table I. The main features are as follows:

The *main updraught and its inflow* (red arrow labelled U1 to U4), consisting of relatively warm, moist air[†] which flows gently towards the approaching storm and then ascends, partly slantwise, and partly vertically as convective plumes, to create a region of precipitation between R1,R2 and R3,R4. The inflow may at times have been split into two layers of higher wet-bulb potential temperature (theta-w) but this detail is omitted from the diagram. Some shallow convection breaks out prematurely ahead of the main updraught above U2 and U3.

The *rear-inflow jet,* corresponding to the main limb of slantwise downdraught (blue arrow labelled D1-D2), air at the leading edge of which impacts on the undercurrent.

The *undercurrent* (green arrow labelled S1 to S6), consisting of cool air in the lowest levels, flowing strongly against the storm's direction of travel. The green arrow, as drawn, also includes a layer of relatively warm but dry (and hence low theta-w) air that caps the undercurrent air. The undercurrent (with its capping layer) deepens beneath the main updraught, its depth being modulated by waves (crests at S3, S4), but it becomes much shallower beneath the impacting rear-inflow jet, where its interface with the overlying jet is characterised by billows (K1-K2).

The *wind-direction anomaly (WDA)*, within the dashed line, W1, W4, W2, corresponding to a region of backed flow within the deeper part of the undercurrent and associated with a positive surface-pressure anomaly between P1 and P2.

Some interpretations and implications of the structures shown in Figure 1 are discussed in section 9, and the conclusions of the paper are presented in section 10.

2. The observations and their locations with respect to the MCS

The MCS affected southern England during CSIP on 24 June 2005. It is the system referred to as MCS 'C' by Browning *et al.* (2010), who showed it to be one of several MCSs that occurred on the northern side of a shallow depression centred over northern France. The MCS passed directly over the CSIP observational network (Browning *et al.*, 2007), with Figure 2 showing the locations of the observations used in this study. The central facility for CSIP was located at Chilbolton and it included a dual-wavelength, scanning Doppler radar, the coverage of which is indicated by the 95 km radius circle. This radar can transmit at both 3 GHz (S-band) and 1275 MHz (L-band), though only the dual-polarisation S-band system was used in this study (Goddard *et al.*, 1994). This radar has a 25 m diameter dish and transmits a peak power of 560 kW, resulting in a sensitive system with an angular resolution of 0.28°. It is capable

[†]A representative radiosonde sounding is shown in Fig. 4 of Browning *et al.* (2010) and representative aircraft soundings are presented later in the paper (Figure 15).

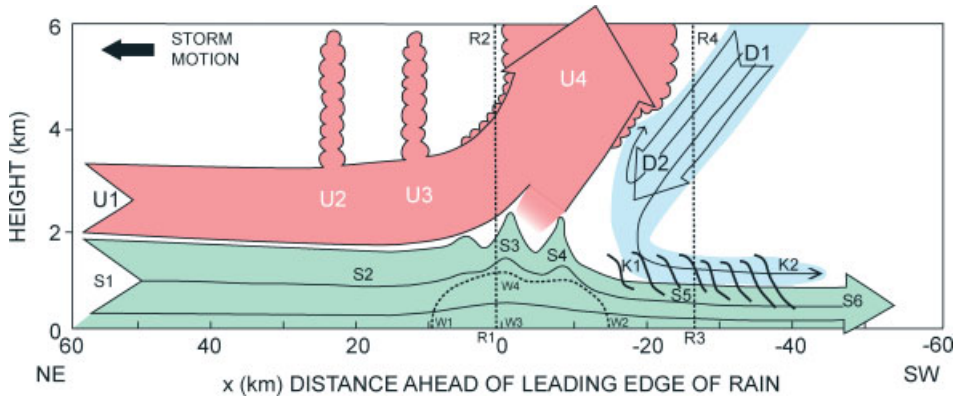

Figure 1. Schematic of the structure of the various features of the MCS, and the wave beneath it, that are inferred from the synthesis of observations described in this paper. Labels are defined in the text and in Table I. Arrows indicate system-relative flows.

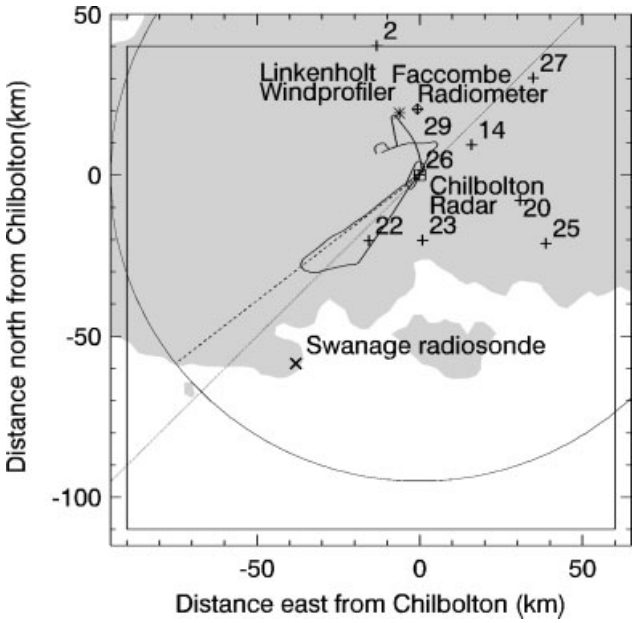

Figure 2. Locations of observing systems used (grey shows land and the rectangle shows the area of each panel of Figure 3). The Chilbolton radar is shown by a square, with the circular arc showing its 95 km range limit. The location of the 232° RHI in Figure 16 is shown by the dashed line. The dotted line shows the direction of travel of the MCS over Chilbolton and corresponds almost to the radar sections shown in Figures 7 to 9. The wind-profiler at Linkenholt is shown by an asterisk and the radiometer at Faccombe by a diamond. Automatic weather stations (AWSs) are shown by plus signs, together with the station numbers referred to in the text. The solid line shows the aircraft track.

of resolving the fine-scale structure of clear-air echo layers within the undercurrent as well as the echo from the nearby heavy rain. The scanning strategy employed a series of 20 RHI (range height indicator) scans, approximately evenly spaced throughout 360° in azimuth followed by low-level PPI (plan position indicator) scans with a cycle time of approximately 40 min.

A wind-profiler radar owned by the Facility for Ground-based Atmospheric Measurements (FGAM) was operated by the University of Manchester at Linkenholt, about 20 km north-northwest of Chilbolton. This is a 3-panel 1290 MHz (UHF) Doppler radar system designed by Degreane Horizon to measure the signal intensity and wind speed and direction twenty-four hours a day under almost all weather conditions. Like the Chilbolton radar, it detects not only hydrometeors but also clear-air refractive index inhomogeneities. It was used to provide wind profiles at 1 min intervals over the height range 200 to 3000 m (subject to errors during some periods of rapidly varying precipitation intensity).

About 20 km north of Chilbolton, at Faccombe, the University of Salford operated a microwave radiometer supported by FGAM. This so-called RPG-HATPRO profiler system, manufactured by Radiometer Physics Gmbh, can retrieve both temperature and humidity profiles, but only the humidity profiles are used here. Profiles of water vapour mixing ratio (WVMR) can be retrieved with an accuracy of 1.0 g m^{-3} and with a vertical resolution of 200 and 400 m over altitude ranges 0–2 km and 2–6 km, respectively, but retrievals are not made in precipitation (Rose *et al.*, 2005).

Automatic Weather Stations (AWSs) were operated at Faccombe by the University of Salford and at many other locations by the University of Leeds (plus signs in Figure 2). We make use of the records of pressure, temperature, water vapour mixing ratio (WVMR), and wind speed and direction from 9 AWSs (the AWSs at Faccombe and Chilbolton also included rain-gauges). Observations of downwelling solar radiation were available at Chilbolton (10-second time-resolution) as well as surface sensible and latent heat fluxes, observed (with half-hour time-resolutions) using eddy correlation (Andreas *et al.*, 2005; Kalthoff *et al.*, 2006) by the University of Karlsruhe.

A Dornier 128 research aircraft (Corsmeier *et al.*, 2001) was operated out of Thruxton airport, about 15 km west of Chilbolton, by the Institute of Flight Guidance and Control of the University of Braunschweig in cooperation with the University of Karlsruhe and Forschungszentrum Karlsruhe. It made a profile within the undercurrent near Chilbolton and then, from the top of this profile, flew horizontal legs within the undercurrent approaching the front of the storm, entering the storm's precipitation, and returning towards Chilbolton. It then climbed to 3000 m before descending to land. Airborne measurements used in this study are of temperature, humidity, wind speed and direction, vertical velocity and shortwave radiation. Videos from the cockpit were used to detect when the aircraft was flying in precipitation. Water vapour was measured by both Lyman-Alpha and HumiCap instruments. A filtered combination of these gives the best estimate of WVMR. Unfortunately, during CSIP IOP3, the Lyman-Alpha failed as the Do 128 entered the wave in the undercurrent, limiting the accuracy of WVMR after this point. The Lyman-Alpha was restarted at the end of the horizontal leg and after this

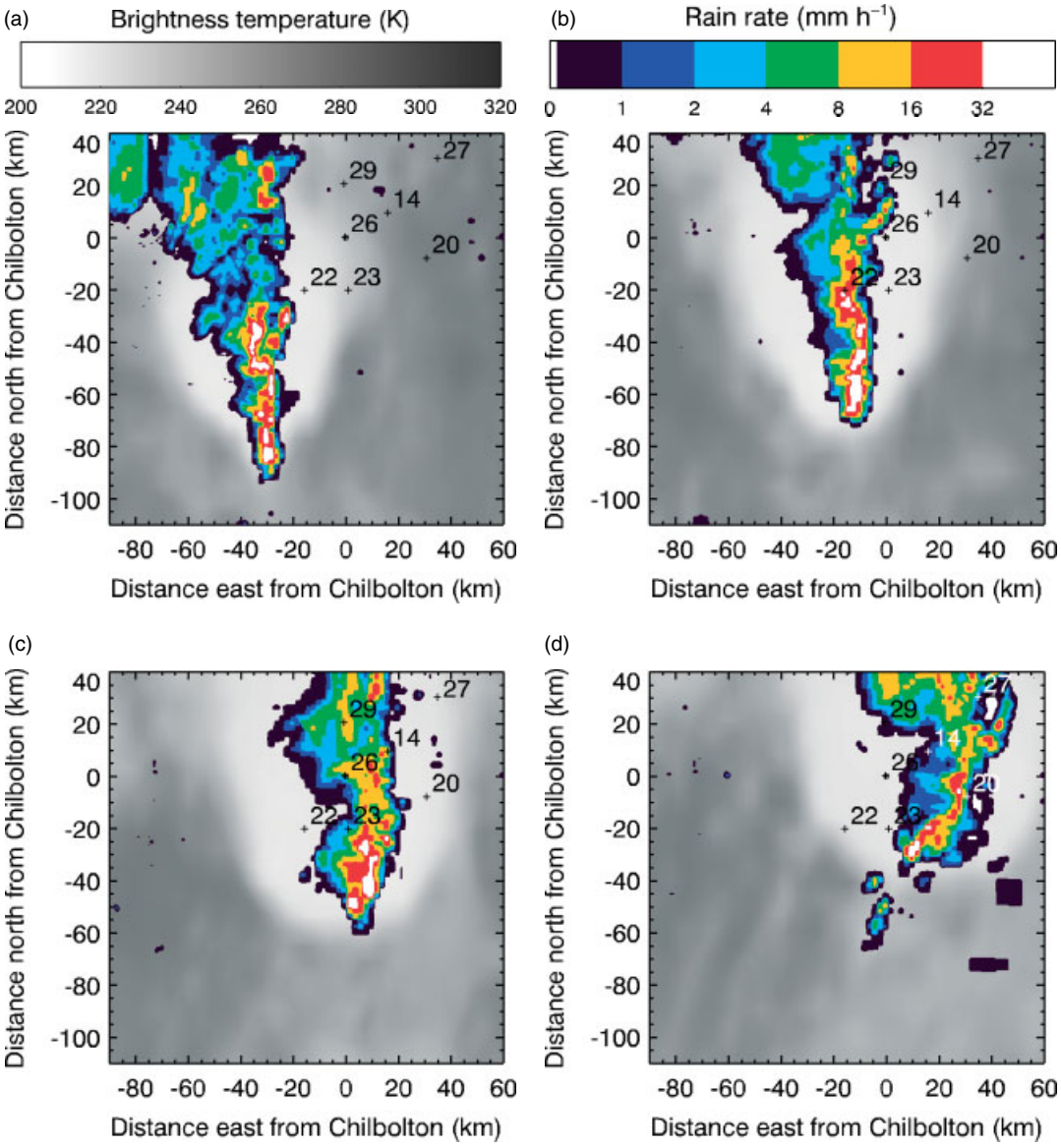

Figure 3. Rainfall rates retrieved from the network radars (coloured) and Meteosat 11 μm brightness temperatures (grey-scaled) at (a) 1230, (b) 1300, (c) 1330 and (d) 1400 UTC, showing MCS C travelling through the observational network during this period. AWS locations are shown by plus signs. An 18 km parallax correction has been applied to all the Meteosat data to allow for the 11 km cloud top.

time the data using the filtered combination of the Lyman-Alpha with the HumiCap gave good agreement with the earlier profile (shown in Figure 15), showing that the restart was effective. When both instruments were operating, the standard deviation of the difference between the HumiCap and the best estimate WVMR was 0.64 g kg^{-1} on one-second data and 0.60 g kg^{-1} on one-minute data; the best–estimate value was on average 0.01 g kg^{-1} moister than the HumiCap value.

The above measurements were supplemented by routinely available cloud imagery from the European geostationary satellite, Meteosat, and rain maps from the UK weather radar network.

3. Surface observations during the passage of the MCS

Figure 3 presents four blended radar/satellite pictures at 30 min intervals from 1230 to 1400 (all times are UTC which is close to local solar time) showing the passage of MCS C over the observational network. The satellite imagery has been shifted 18 km southwards to correct for the parallax from a cloud-top height of 11 km. The rectangle drawn within Figure 2 shows the area covered in each frame of Figure 3. The MCS was travelling north-eastwards across the AWS network at 15 to 16 m s^{-1} between 1230 and 1400, the main focus of the study being just after 1300 when the MCS was passing over the Doppler radar and wind profiler, and just before 1230 when the aircraft was measuring the undercurrent ahead of it.

Precipitation echo associated with MCS C was, according to the radar-network data, overhead of Chilbolton from about 1305 to 1350. Heavy rain was measured at the surface at Chilbolton between 1318 and 1336 (Figure 4, AWS site 26). Figure 4 shows that the storm was accompanied by a positive pressure anomaly, which started at about 1245, before the arrival of the surface rainfall, and ended at about 1330 while it was still raining heavily. A small local minimum in surface pressure of approximately 10 min duration was observed immediately after the positive pressure anomaly. This meso-high–low pair appears similar to those generated

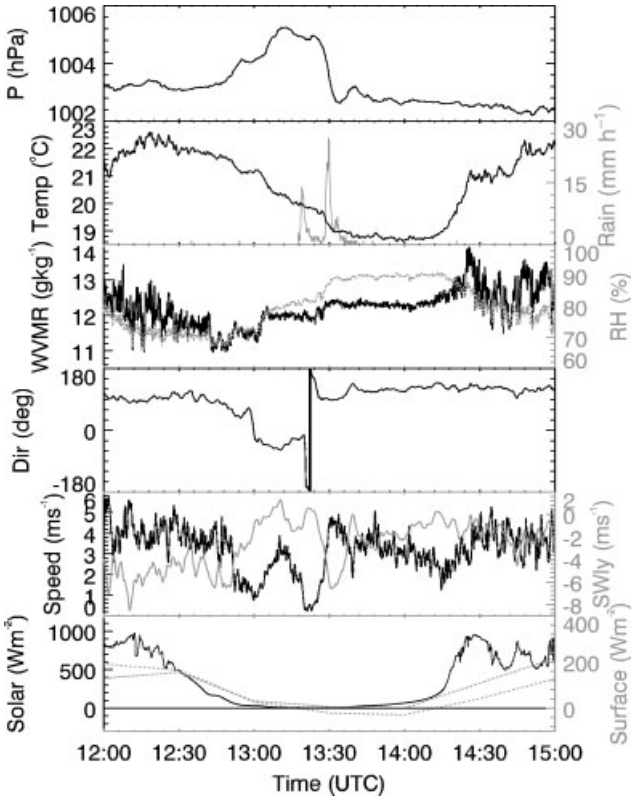

Figure 4. Surface weather station data from Chilbolton (station number 26, 3-second data) before, during and after the passage of MCS C. Time series of pressure, temperature, rain-rate (grey line), water vapour mixing ratio, relative humidity (dashed grey line) wind direction, wind speed, southwesterly wind speed (grey line) downwelling solar flux (10-second data), surface sensible heat flux (dashed grey line, 30-minute data) and surface latent heat flux (dash-dotted grey line, 30-minute data) are shown.

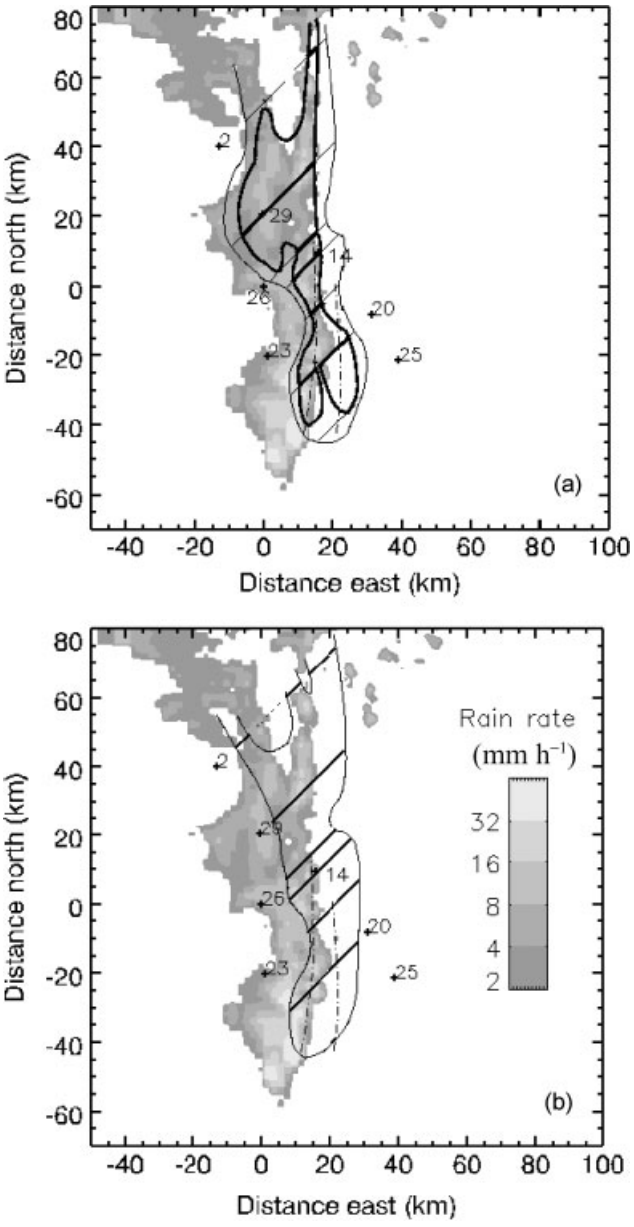

Figure 5. Rainfall intensity (grey-scaled, from network radars) for MCS C at 1330 UTC, with the locations of AWS sites 2, 29,14, 26, 20, 23 and 25 indicated by + signs. Time–space converted bars, which are then contoured, show (a) the pressure anomaly (with thin lines for 1.5 hPa and thick lines for 2 hPa), and (b) the wind direction anomaly (WDA). The dash-dotted lines, AB and CD, from Figure 6 are superimposed in both plots.

by low-level cooling in an idealised model and discussed by Haertel and Johnson (2000). However, the analysis in this paper shows that the pressure anomalies here can be largely explained by the hydrostatic effect of variations in the undercurrent depth (section 9.1) rather than diabatic cooling.

The MCS was also characterized by a pronounced wind-direction anomaly (hereafter WDA) in which the predominantly easterly flow within the undercurrent was interrupted by a 20 min period of north-westerly winds. Wind speed remained around 4 m s^{-1} but it dropped to almost calm around the times of the wind reversals. This behaviour was reproduced at all of the AWS sites shown in Figure 5 and is consistent with a near-linear transition between the easterly wind vectors outside of WDA and the more nearly westerly wind vectors within it. The time of the WDA, 1300 to 1320, coincides with the earlier part of the storm, beginning just ahead of the rain and ending as the storm core passed over. The overall period of the surface-wind perturbation, i.e. including the parts of the lulls extending beyond the boundaries of the WDA, was from 1250 to 1330, corresponding roughly to the duration of the positive surface-pressure anomaly. The wind-speed component in the direction of the southwesterly system velocity is well correlated with the surface pressure anomaly (a correlation coefficient of 0.78 for 1245 to 1345) as expected from Coleman and Knupp (2009). These anomalies will be shown to be closely associated with, and probably largely due to, the wave in the cool undercurrent.

The relationship between surface wind, pressure and rainfall, just described, tended to apply along much of the north–south extent of the MCS, at least at 1330, for which time we have performed a spatial analysis (Figure 5). In Figure 5 the time records from seven AWSs have been converted to spatial plots assuming a system velocity of 60 km/h from 225° and the regions where the threshold values were exceeded are indicated by lines orientated along 225–045°. The tendency for the surface-pressure maximum to occur at the leading edge of the rain is evident in the southern half of the MCS, but in the northern half the positive pressure anomaly is seen to have been sustained throughout the longer period of rain (Figure 5(a)). The tendency for the WDA to coincide with the leading edge of the heavy rain is well defined in Figure 5(b).

An interesting detail in Figure 5(a) is the tendency for the pressure anomaly to have two maxima. In the northern half

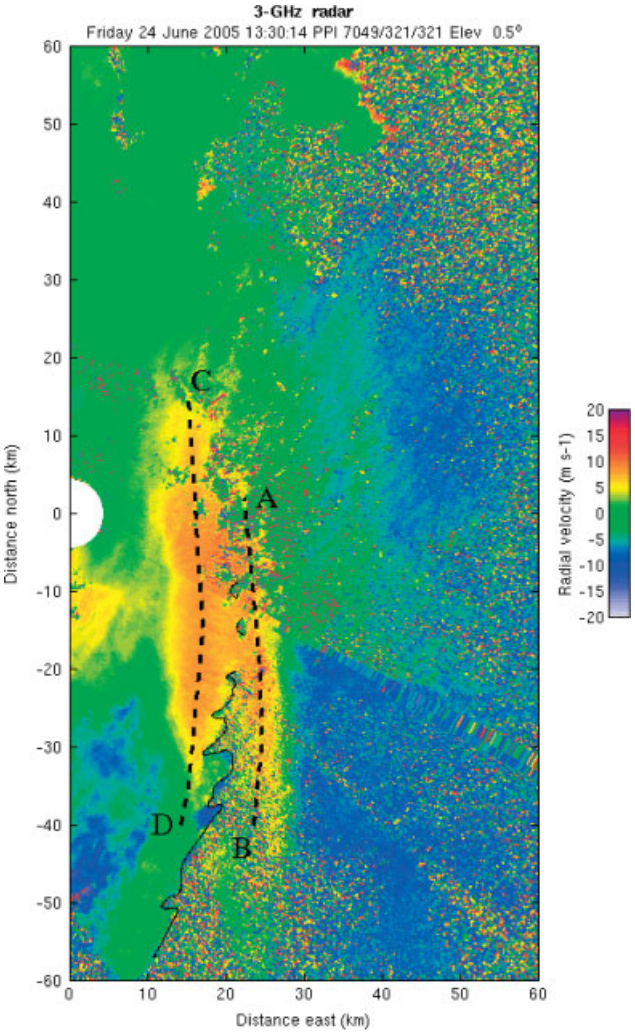

Figure 6. Chilbolton Doppler PPI showing radial velocity (m s^{-1}, positive away from the radar) for the eastern half of the PPI, derived by combining the PPI sector-scan at 0.5° elevation (starting at 1330:13 at azimuth 0°) with the PPI sector-scan at 1.0° elevation (starting at 1332:25 at azimuth 118°, the higher elevation for this scan being necessary because of the poorer horizon in the southern sector). The velocity scale is given by the colour bar; speckled colours indicate noise due to weak signal. The dashed lines, AB and CD, and the thin solid black line are discussed in the text.

of the MCS this appeared to be associated with the formation of two north–south bands of heavy rain. In the southern half of the MCS there is less evidence of a double rain-band but there is still evidence of two pressure maxima. These appear to correspond to the dash-dotted axes in Figure 5, which were derived from the axes of maximum radial-outward winds measured in an almost coincident radar PPI, shown in Figure 6. Although there is no evidence of a double structure in the wind-direction records from the AWSs in Figure 5(b), the double structure (i.e. dashed lines AB and CD) is clearly evident in the line-of-sight Doppler-radar PPI plot in Figure 6. (There is a 3 km displacement of the axes AB and CD between Figures 5 and 6 because of the 3 min difference between the times of the appropriate part of the PPI scan in Figure 6 and the plots in Figure 5.)

The PPI plot in Figure 6 was reconstructed from two PPIs, with the main portions of the dashed axes AB and CD detected in the second PPI. At the appropriate ranges of 30 and 50 km, the two PPI scans would have been 500 m and 800 m above the surface, respectively. Thus, although there was no evidence of double structure in the WDA measured at the surface by the AWSs, the double structure evidently did exist between 500 and 800 m. In other words, the WDA extended above 500–800 m along the axes, AB and CD, separated by about 7 km, but it was restricted to the lowest several hundred metres in the zone between AB and CD. The fact that the double structure appears to be reproduced in the pattern of the surface-pressure anomaly indicates a close relationship between the pressure anomaly and the depth of the overlying WDA. In later sections we shall present vertical cross-sections from radar data to show that the WDA occurred where undercurrent air was being lifted within a wave, thereby suggesting that the pressure maximum at the surface was, at least in part, a hydrostatic effect where the depth of the overlying cool undercurrent air was increased.

Another intriguing feature of Figure 6 is the shape of the boundary of detectable echo, highlighted by the thin black line along the leading edge of the WDA crest labelled CD. This boundary corresponds to the top of the clear-air echo associated with the undercurrent. The wavy nature of this boundary suggests the existence also of secondary waves on a scale smaller than the 7 km spacing between the main wave crests AB and CD.

Changes in surface temperature and humidity during the passage of the MCS were gradual and sustained over a longer period than the pressure and wind anomalies. The temperature dropped steadily from 22.5°C at 1227 to 18.8°C at 1333. The relative humidity increased from 70 to 90% over the same period. The fluxes plotted in Figure 4 exhibit a relatively prolonged minimum (the minimum observed value of the downwelling solar flux was 5 W m^{-2}) corresponding to the rather long period of lowered temperature and raised humidity. This evidence, combined with similar data from other AWS sites, is used in section 7 to show that the changes in temperature were largely due to decreases in surface fluxes that were caused by the effect of cloud cover on insolation rather than to rain evaporation or the wave in the undercurrent. Previous studies within CSIP have demonstrated the kind of surface effects that can be caused by the shading from anvil cloud (Marsham *et al.*, 2007a, 2007b).

4. Vertical structure of the undercurrent wave as revealed by the Doppler radar

In this section we present RHI scans from the high-resolution Doppler radar at Chilbolton to reveal the vertical structure of MCS C within the lowest 6 kilometres. The scans, presented in Figures 7 to 9, were obtained close to the time when the MCS was affecting the other observing systems as described in sections 3 and 5 – in fact, when the MCS was almost directly overhead of Chilbolton. One might have thought that this would have been a bad time to exploit RHI scans because part of the storm directly overhead was unobserved. On the contrary, however, by combining two RHI scans, one made to the south-west (strictly 221°) at about 1313 and the other made towards the north-east (044°) at about 1327, it has been possible to obtain a good description of the structure on both sides of the storm at the low levels that are most relevant to the present study. Moreover, by adjusting the positions of both scans to a common time of 1320, the size of the unobserved 'blind' area just above the radar is reduced, i.e. the earlier upstream scan is shifted forwards by about 7 km into the blind area whilst the later downstream

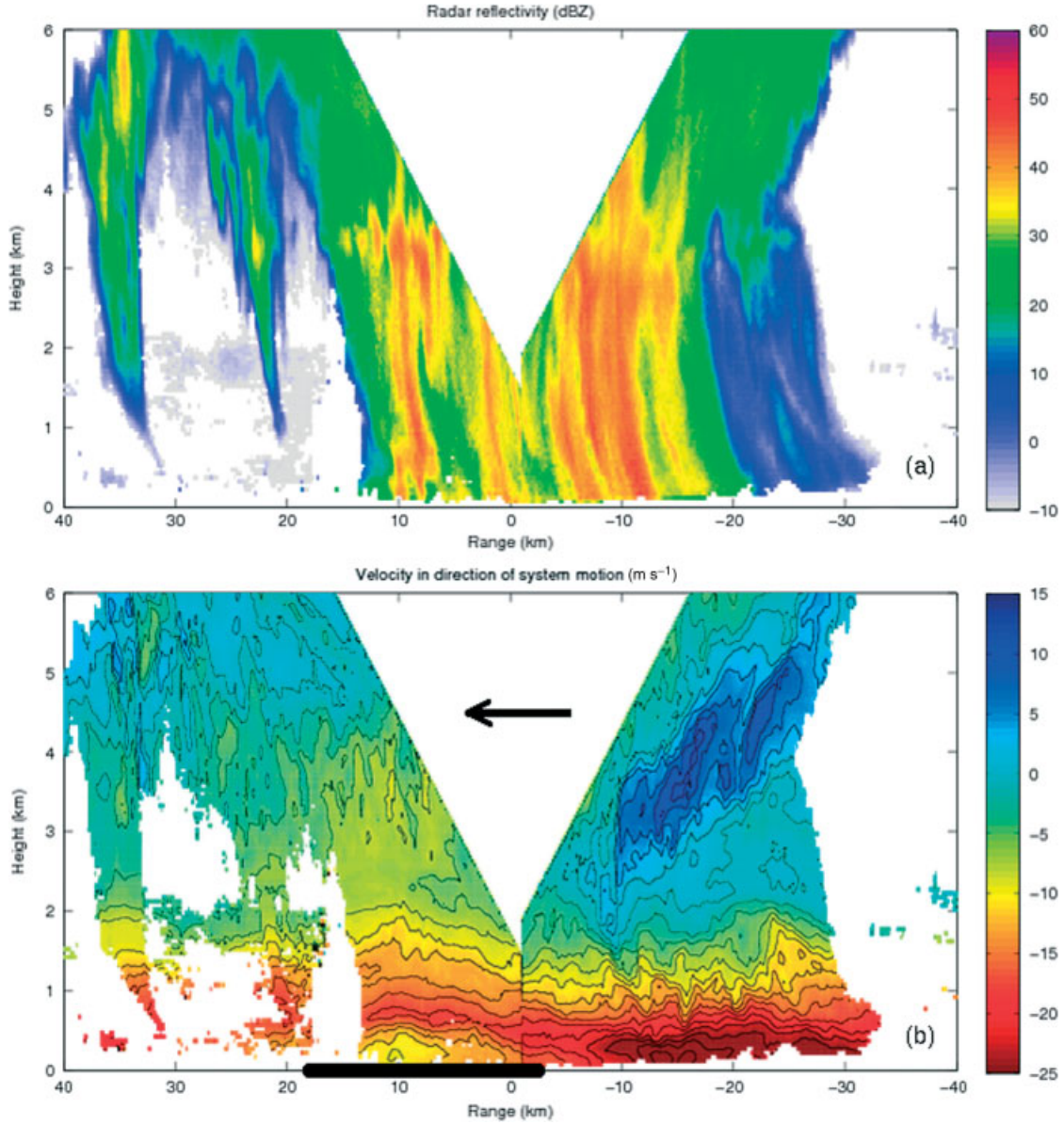

Figure 7. Back-to-back RHIs from the Chilbolton Doppler radar along 044°(left)/221°(right) adjusted to a common time of 1320 UTC when the core of the MCS was directly over the radar (the storm was travelling from right to left). (a) Reflectivity (dBz, colour shading), (b) storm-relative velocity component (colour shading plus black contours at 2 m s^{-1} intervals, positive in the direction of the storm's travel). Using a system velocity of 16 m s^{-1} from the southwest, the time–space adjusted duration of the WDA from the Chilbolton AWS is shown by the thick black line below (b). The bold arrow in (b) shows the direction of the system velocity.

scan is shifted backwards about 7 km into the blind area. As we shall see, despite the time difference between the scans, the data from these two scans fit together remarkably well and provide almost complete coverage below 2 km. Only above 3 km is the blind area greater than 10 km across. We shall refer to the combined scan as a back-to-back scan.

Figure 7 shows the back-to-back RHI scan at 1320. The storm at this time was travelling at 16 m s^{-1} towards the north-east (left side of the figure) and positive velocities in Figure 7(b) correspond to a component of storm-relative flow in this direction. Thus the shades of blue represent flow overtaking the storm, whilst the red, yellow and green colours represent flow against the storm's direction of travel. The darker blue shading in (b) clearly highlights the rear-inflow jet descending slantwise into the region of heaviest rain as shown by the red shading in (a).

In the undercurrent below about 2 km the flow against the storm's direction of travel (warm colours in Figure 7(b)) is seen to become increasingly strong at levels closer to the ground beneath the rear-inflow jet, reaching 26 m s^{-1} relative to the storm at levels below 400 m above ground level. On the forward side of the storm, the flow in the lowest 500 m of the undercurrent decreases to 12 m s^{-1} relative to the storm (yellow shading in Figure 7(b)). This region corresponds to the WDA detected at the surface by the Chilbolton AWS – see the bold black line plotted at the surface in Figure 7(b). Above the (yellow) WDA in Figure 7(b), the velocity contours are seen to bow upwards. We shall show that this is a region where the undercurrent flow also bows upwards in association with the undercurrent wave. The strong diffluence in Figure 7(b) at ranges between −10 and +10 km (with a change of 14 m s^{-1} over 20 km at a height of 400 m, corresponding to a component of divergence of 7×10^{-4} s^{-1}) implies a region of pronounced descent in the undercurrent where the rear-inflow jet appears

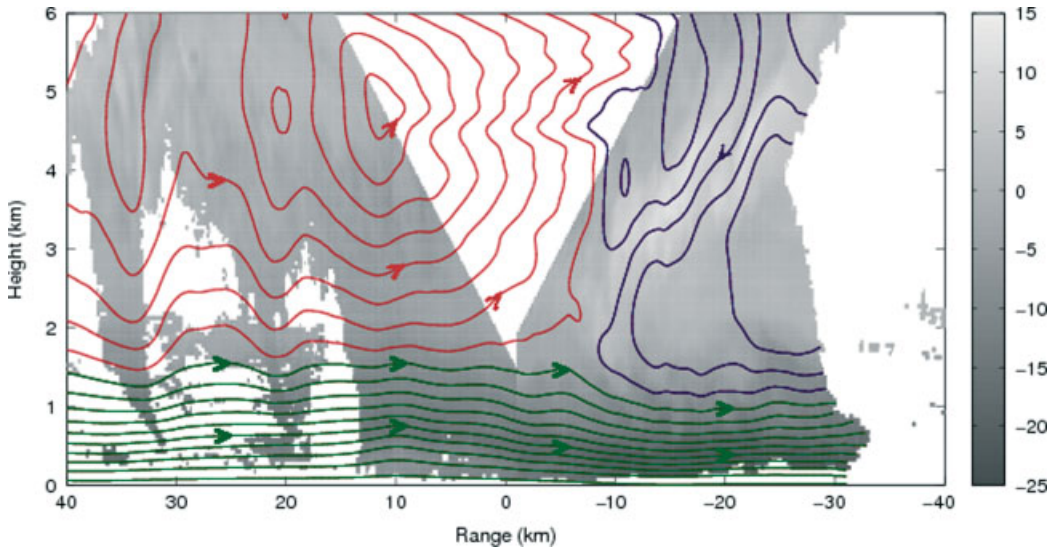

Figure 8. Streamlines for same area as Figure 7, derived from the Doppler velocity plot in Figure 7(b) which is reproduced here as a grey scale. Red, blue and green streamlines, respectively, represent air flowing in and towards the updraught, air in and leaving the rear-inflow jet, and air within the cool undercurrent and its warm, dry capping layer. The streamlines have been calculated from continuity assuming two-dimensional flow. The calculations also assume that the Doppler velocity gives the true horizontal component of the wind within the section; this is valid to a good approximation within the undercurrent, and is valid to within 3% at the top of the RHI scans for horizontal flow, but is worse in a few locations near the tops of the scans where there are significant vertical motions.

to be compressing the undercurrent on the rear side of the wave.

Figure 8 shows a streamline analysis derived, assuming two-dimensional (2-d) continuity, from the field of the horizontal wind component obtained from Figure 7(b). The derivation neglects contamination of the Doppler velocity by the vertical motion of scatterers; vertical velocities of, for example, 5 m s^{-1} would produce errors of 1.3 m s^{-1} at the top of the 15° RHI scans but velocities in the low-level undercurrent would be relatively unaffected. Horizontal smoothing over 3 km and vertical smoothing over 200 m has been applied to remove small-scale features which are liable to be more transient. Directly above the radar, the accuracy is poorer because of the interpolation required across the blind area; fortunately the blind area does not extend into the undercurrent. Although we shall present other data shortly which are believed to give a more dependable picture of some aspects of the detailed flow, the streamline patterns in Figure 8 are qualitatively credible. Thus, for example, the rear-inflow jet (blue streamlines) can be seen descending parallel to the axis of the strongest rear-to-front storm-relative winds (the palest grey shading in this figure). The upper part of the rear inflow appears to be detrained and to ascend at the lower edge of the main updraught (red streamlines). The lower part of the rear-inflow jet gives the appearance of pushing down on the underlying undercurrent (green streamlines) before turning around and flowing rearwards (relative to the storm) just above the undercurrent.

Air in the undercurrent itself, as seen in Figure 8, ascends a little as it approaches the front of the storm (left of the diagram), before reaching a maximum height at range −10 km, where the dark grey shading shows the upward bowing in the Doppler-velocity contours referred to earlier. It then finally descends strongly in the region where the rear-inflow jet appears to be compressing the undercurrent. Specifically, the second green streamline above the ground ascends from 200 m at range +40 km to 300 m at +10 km, before descending to 120 m at −15 km. Similarly the fourth green streamline above the ground ascends from 440 m to 630 m before descending to 260 m. The eighth green streamline ascends from 1070(+/−80) m (between +40 and +30 km) to 1200 m before descending to 650 m. The top green streamline ascends from 1510(+/−170) m to 1520 m before descending to 970 m.

Another, and more reliable, indication of the shape of the undercurrent wave (at least where the echo intensity is sufficiently strong, i.e. to the right of +13 km) is provided in Figure 9. This figure depicts (a) the spectral width, which is dominated by turbulence and wind shear within each pulse volume, and (b) the vertical shear of the Doppler velocity, for the same scan as shown in Figure 7. In regions such as the undercurrent where there is no deep convection, both of these products are an indication of the stratification of the atmosphere: shear tends to accumulate where the static stability is strong enough to sustain it, and Kelvin–Helmholtz instabilities and significant turbulence develop in the shear layers where the Richardson number decreases to 1/4 over all or part of the layer. The Chilbolton radar, with its 25 m diameter dish, is particularly effective at resolving this layering because of its narrow (0.28°) beam-width. Whereas the pattern of clear-air echo layers in other radar scans where the layer echoes are more detectable (e.g. the later Figure 10) shows that the stratification within the undercurrent is more or less horizontal far away from the MCS, Figure 9 shows that in and near the storm, where the undercurrent is perturbed by the storm dynamics, the layering follows the pattern of the resulting wave disturbance.

We shall consider two of the more distinctive layers in Figure 9. One of these is the layer of maximum negative shear (dark blue layer in Figure 9(b)) which also shows up as a layer of maximum spectral width (green in Figure 9(a)). This depicts the undercurrent flow ascending from about 500 m at +20 km to a maximum height of 600 m at +10 km before descending to a minimum of about 120 m at −15 km. This small rise, followed by a strong descent beneath the impacting rear-inflow jet, is broadly similar to the behaviour

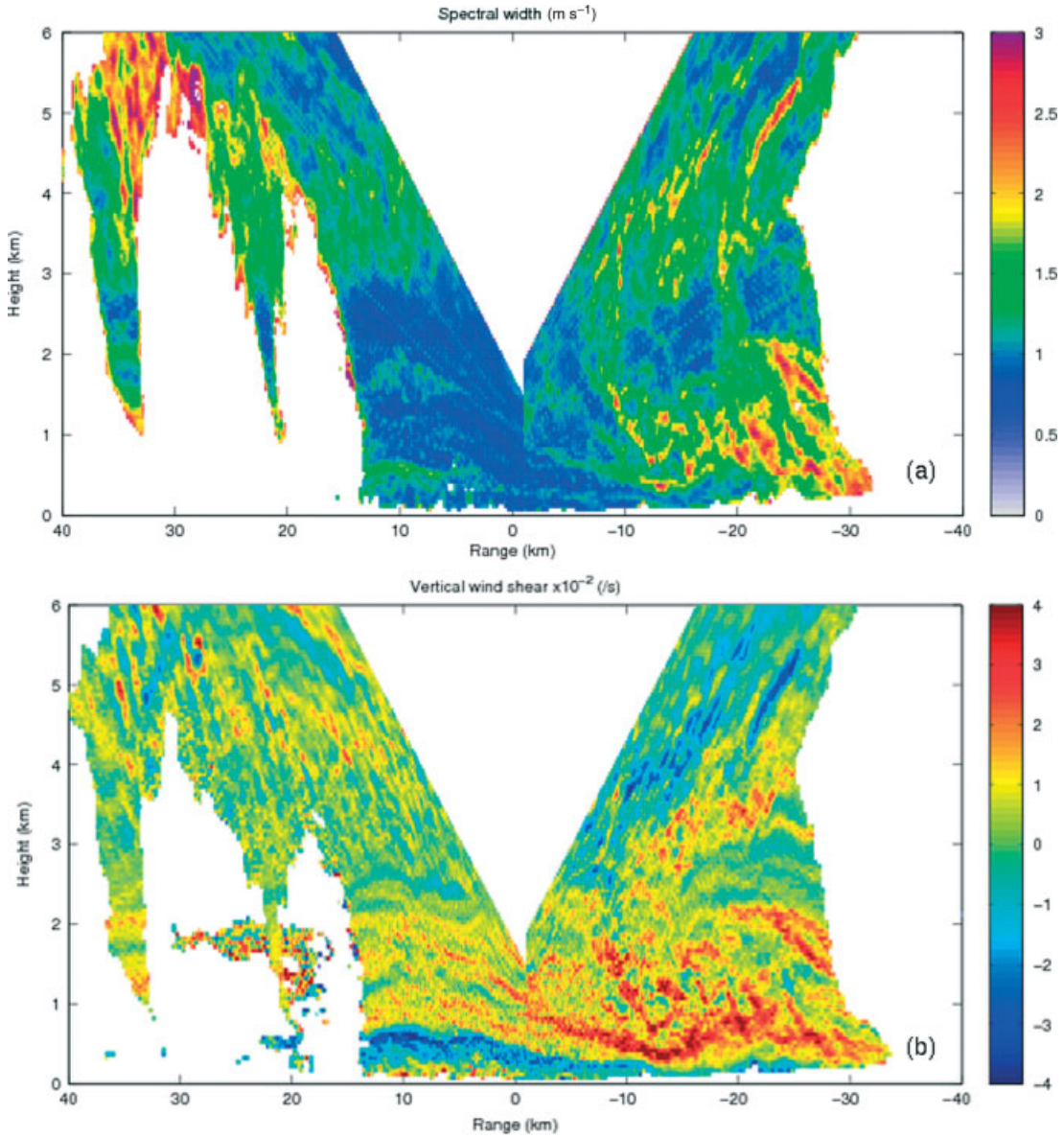

Figure 9. As Figure 7, but for (a) spectral width (colour shading) and (b) wind shear (colour shading).

of the fourth green streamline in Figure 8 referred to in the previous paragraph, its ascent from 440 m to 630 m followed by descent to only 260 m comparing reasonably well with the ascent from 500 m to 600 m followed by descent to 120 m in Figure 9. This supports the validity of the 2-d assumption in deriving streamlines in the lower part of the undercurrent.

The other distinctive layer within the undercurrent that we shall consider is the layer of maximum positive shear (orange and red in Figure 9(b)) that peaks at 1900 m at +10 km before descending to 350 m at −13 km where it changes from orange to dark red owing to a near-doubling of the shear. This layer shows up as a green layer of maximum spectral width in Figure 9(a) which becomes yellow and red (increasing spectral width) where it descends to its lowest level. The increase in spectral width is due partly to the increase in shear, and perhaps partly also to an increase in turbulence caused by the increasing shear. (As discussed shortly, the general region of the undercurrent beneath the impacting rear-inflow jet was characterized by intense turbulence.) This layer, with its very large vertical excursion from 1900 m down to 350 m, was not reproduced well in Figure 8, where the topmost green streamline descends from 1520 m down to only 970 m and streamlines at and above 1900 m ascended as part of the main updraught. Therefore, in the upper layers of the undercurrent the 2-d assumption was less valid than it was for the lower part.

In summary, the undercurrent in the part of the storm observed with the Chilbolton radar deepened as the air approached the front of the storm. It then accelerated and became much shallower under the leading edge of the descending rear-inflow jet, which gave the appearance of being responsible for compressing the undercurrent where it impacted upon it. Not only did it appear to compress the undercurrent flow and cause it to accelerate, but the resulting increase in shear also led to the occurrence of shearing instability in the form of what appeared to be large-amplitude Kelvin–Helmholtz billows. The billows show up in Figure 7(b) as undulations in velocity with axes of velocity maxima inclined upwards from right to left with a slope of between 1 in 3 and 1 in 4. The billows show up in Figure 9(a) and (b) as characteristically sloping shear

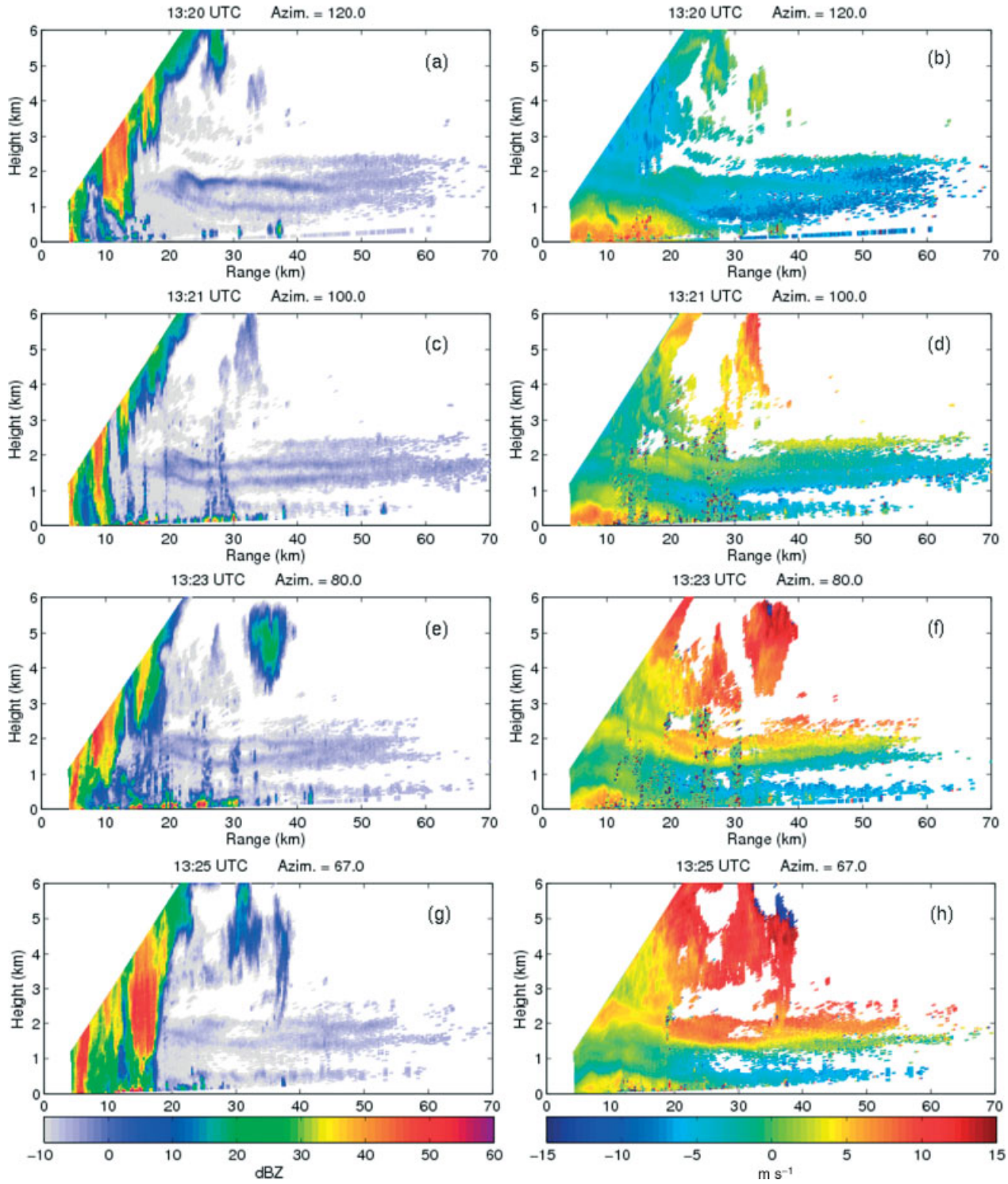

Figure 10. RHIs from the Chilbolton radar showing the front part of the MCS and the inflow region ahead of it. Plots in the left column ((a), (c), (e) and (g)) show reflectivity; those in the right column ((b), (d), (f) and (h)) show Doppler winds. Plots in the top row ((a), (b)) are towards 120° at 1320:27 UTC; second row ((c), (d)) are towards 100° at 1321:59; third row ((e), (f)) towards 080° at 1323:47; and fourth row ((g), (h)) towards 067° at 1325:13. The MCS was moving from left to right (unlike in other plots).

layers similar to, although rather more chaotic than, those observed by Chapman and Browning (1997 – see their Fig. 4(c)). The chaotic nature of the present billows may be due to spatial variability in forcing by the impacting rear-inflow jet. The apparent wavelength of these billows, as seen in Figures 7(b), 9(a) and 9(b), is about 3 km (or even less if the billows were not orientated perpendicularly to the scan) and their crest-to-trough amplitude is of order 1 km.

In Figures 7, 8 and 9, the data used to show the existence of only slight ascent within the undercurrent ahead of the storm would have been less reliable than the data obtained in other parts of the undercurrent because of the large areas of weak or no echo that had to be interpolated across. Further evidence from the Chilbolton radar, presented next, suggests that in some places there was in fact substantial ascent ahead of the storm. Figure 10 shows four successive scans made just before the left-hand scan in Figures 7 to 9; however,

note that since these four scans were towards the east, the orientation of Figure 10 is such that the storm motion is now with a component from left to right rather than right to left as in the preceding figures. The advantage of the scans in Figure 10 over those in Figures 7 to 9 is that, as already alluded to, the intensity of the clear-air echo within statically stable layers in the lowest 2 km is now sufficient to reveal the form of the undercurrent flow reliably from close to the storm to ranges a long way ahead of the storm.

The data in all the panels in Figure 10 imply strong ascent within the undercurrent in the 20 kilometres ahead of the storm core. The ascent shows up both in the shape of the clear-air echoes associated with statically stable layers in the undercurrent and in the shape of the corresponding velocity contours. The velocity plots give the more complete picture of the flow close to the storm. There are two reasons for this. Firstly, the Doppler velocity plots reveal the flow even where intense echo from rain obliterates the clear-air echoes that are used to infer flow in the reflectivity plots. Secondly, as the radar alternates from horizontal to vertical polarisation from pulse to pulse, the Doppler velocity data benefits from using both polarisations, essentially doubling the number of pulses and thereby enhancing coverage in areas of very weak reflectivity. The velocity plots suggest that the height through which the undercurrent ascends just ahead of the storm (between radar ranges of about 28 and 8 km) is typically 700 m. However, one might expect the velocity contours, whilst giving a useful qualitative indication of flow, would underestimate the vertical displacement of streamlines where the storm-relative velocity decreases with height; this is because of the deceleration that is likely to occur along a streamline where the flow deepens. Examination of the steepest clear-air echo layers in Figures 10(c) and (e) supports this interpretation, suggesting ascent of as much as 900(+/−50) m between ranges of 28 and 15 km.

Another interesting aspect of Figure 10 is that although there is strong ascent over a 20 km zone (roughly 8 to 28 km range) just ahead of where the rain reaches the ground, farther ahead of the storm core there is evidence of substantial initial descent as the undercurrent air approaches the storm (from right to left in the figure). For example, Figure 10(c) shows a clear-air echo layer descending by 500 m, from 1650 m at radar range 68 km to 1150 m at range 28 km, before rising steeply to 1700 m at 18 km range. This behaviour accords with that inferred from a radar scan at the earlier time of 1155 (see Figs. 8 and 9 in Browning *et al.*, 2010). The observed descent through 500 m over a distance of 40 km applied to precipitation-free air that was approaching the front of the storm at an average storm-relative velocity of 18 m s^{-1}. This implies an average vertical air velocity of about −0.2 m s^{-1}. Dry descent of as much as −0.4 m s^{-1} has been observed in the low troposphere beneath the anvil of a convective storm by Groenemeijer *et al.* (2009). They attributed the dry descent to compensation for the upward mass flux in the nearby convective updraughts (e.g. Marsham and Parker, 2006). Although some of the descent in the present case was beneath the anvil, much of it was somewhat ahead of the leading edge of the anvil.

During the period corresponding to Figure 10, the heaviest rain and the main updraughts aloft (i.e. above the undercurrent) were situated virtually above the radar site; however, incipient updraught cells (cumulus congestus) can also be seen occurring just ahead of the main storm. These cells are revealed in two ways in the reflectivity plots. In Figure 10(c), the edges of the updraught plumes show up as clear-air mantle echoes (Knight and Miller, 1993; Wakimoto *et al.*, 2004) between heights of 3 and 6 km and at a range of around 30 km. In Figure 10(e) and (g), echoes can be seen at the same ranges and levels, but the extent of echo suggests that the interiors of the mantles are now filled by echo from precipitation particles developing within the convective plumes associated with the congestus clouds. The congestus occurred close to where, as noted above, the descent changed to ascent within the undercurrent at the 1150 m level; some of the congestus occurred even ahead of this, where the undercurrent was still descending slightly. However, there is faint evidence, in Figure 10(a) for example, that the descent was less marked in the layers above 2000 m – and this would of course be consistent with the occurrence of the congestus – suggesting that the dry descent discussed above was restricted to a shallow layer in the undercurrent, unlike in the conceptual model in Fig. 16 of Groenemeijer *et al.* (2009) where it extended over a substantial depth below the anvil.

5. Vertical structure of the undercurrent wave as revealed by radiometer and wind profiler

We continue the investigation of the undercurrent wave in this section by showing time–height sections of WVMR in the lowest 6 km measured by the radiometer at Faccombe (AWS Site 29, situated about 20 km north of Chilbolton), and of wind speed and direction in the lowest 3 km measured by the UHF wind profiler at Linkenholt, just 5.5 km west-south-west of Faccombe.

The radiometer time–height section in Figure 11 shows the isopleths of WVMR broadly rising from 1200 until 1304 at which time the instrument stopped recording with the passage of the MCS overhead. The main period of surface rain occurred between 1312 and 1354 but the radiometer did not start recording again until 1500 by which time the isopleths of WVMR had returned approximately to their pre-storm levels. Assuming, to a first approximation, that advection of horizontal gradients of WVMR can be neglected in comparison with vertical displacements of the strong vertical gradients by the undercurrent wave, then the time record can be interpreted as an equivalent spatial cross-section in which the isopleths of WVMR correspond to streamlines of the airflow[‡]. Recalling that the propagation velocity of the MCS was close to 1 km/min, it would appear that the undercurrent air ascended significantly from a position 60 km ahead of the storm (i.e. at 1200) at least until the arrival of the storm interrupted the record (9 min before the onset of heavy rain at the surface).

During the period 1140 to 1200, i.e. between about 70 and 90 km ahead of the onset of rain, Figure 11 suggests that the air in the undercurrent descended by up to about 300 m before it began its ascent towards the storm. This implies a rate of dry descent similar to that inferred in the previous section from Figure 10. Figure 11 also suggests that

[‡]The spreading of the isopleths of WVMR in Figure 11 with time shows either convergence or advection of horizontal gradients in WVMR. The analysis in section 6 shows there were large-scale gradients in WVMR, but evaluating the relative contributions of these two effects to Figure 11 is not possible with the available data.

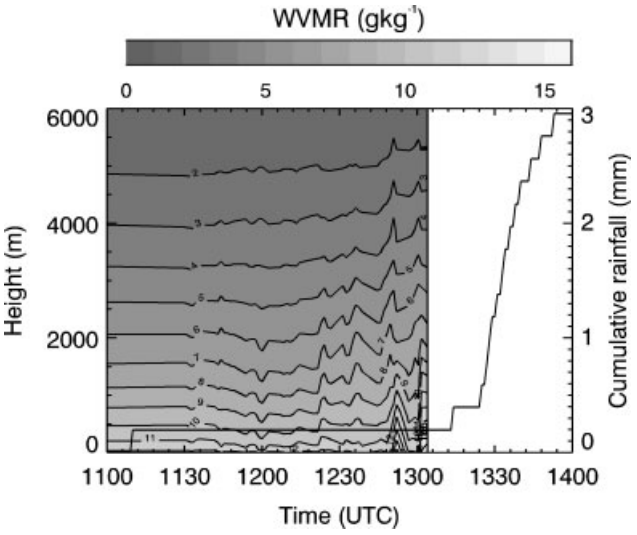

Figure 11. Time series of water vapour mixing ratio profiles retrieved from a vertically pointing radiometer (grey-scaled) and cumulative rainfall from a tipping bucket rain-gauge (thick line) at Faccombe (20 km north of Chilbolton, see map in Figure 2). Water vapour profiles could not be retrieved during rain (masked white).

significant dry descent was limited to the undercurrent below 2000 m, becoming zero at 3000 m and being replaced by ascent at and above 4000 m. During the period 1200 to 1304, ascent was occurring both in and above the undercurrent. Superimposed on the general rising trend, the undercurrent air also appears to have undergone vertical oscillations with a period of 10(+/−5) minutes corresponding to a horizontal wavelength of 10(+/−5) km, or about 7 km resolved at right angles to the north–south axis of the storm core. This wavelength is similar to the spacing of the pair of higher WDA-tops shown in Figure 6. According to Figure 11, the crest–trough amplitude of the oscillations in the airflow close to the ground just before the arrival of the rain area was as large as 1000 m.

Looking at just the overall trend in Figure 11, i.e. smoothing out these short-wavelength oscillations, the general trend was for the undercurrent to deepen by about 700 m over 60 km (i.e. from 1200), most of it over a distance of 40 km, but with shorter-wavelength perturbations superimposed on it, especially in the lowest 1000 m where their amplitude reached +/−500 m. In the previous section we presented radar evidence of 900 m of ascent concentrated in the nearest 20 km, with descent farther ahead of the storm. The discrepancies may be due to spatial or temporal differences between the two sets of observations, or it may be due to a breakdown in the assumption of negligible horizontal advection of WVMR made in the interpretation of Figure 11. Nevertheless, a large amount of ascent seems to be implied as the undercurrent approached the front of the storm.

At Linkenholt, the site of the wind-profiler, the first rain shaft was observed around 1300 and this is the likely cause of wind errors in the profiler record that have been masked (black) in Figure 12. A considerable amount of reprocessing was required in order to reduce the size of the regions having to be masked. At around 1257 and below 800 m the wind profiler shows anomalous southerly winds, just ahead of masked data. It is possible that these too should be masked, but when space–time adjusted these data correspond to the wave crest observed in Figure 11 at 1300 UTC, so may conceivably be real and as a result have been left unmasked.

In Figure 12(a), the height of the area of purple shading, showing air with ground-relative speeds that happened to be close to zero, is seen to increase from about 500 m at 1245 to 1000 m at 1305. This wind-speed anomaly is situated directly above the WDA at the ground as measured by the AWS at nearby Faccombe (bold black line). The wind-direction plot in Figure 12(b) shows ground-relative winds from an easterly or north-easterly direction in the undercurrent in the lowest 500 to 1000 m, except for the anomalous southerlies referred to in the previous paragraph and, more credibly, except also for the period corresponding to the WDA when the winds at some levels below 1000 m are backed to between northerly and westerly. Comparison with Figure 12(a) shows that the winds are light throughout much of the WDA, except below 500 m where they exceed 5 m s^{-1} in places. At 200 m, the lowest level to which the profiler was able to make measurements, the winds backed to approximately north-westerly from 1305 to 1323.

According to Figure 12(b), the WDA was confined mainly to the lowest kilometre, where pressure perturbations are expected to be largest (see discussion in section 9.1). Above this, at heights from 1000 to 3000 m, Figure 12(b) shows a narrower range of wind directions, between southerly (green) and south-westerly (yellow). Significantly, there is evidence of a large-amplitude wave pattern at these levels, with green and yellow features spaced at intervals of about 10 to 12 min. The vertical extent of these fluctuations may have been in excess of 1000 m between 1300 and 1330. The radiometer record in Figure 11 showed undulations in the flow of broadly similar period but their crest-to-trough amplitude over the height interval 1000 to 3000 m was only 100 to 600 m. However, the radiometer record terminated with the arrival of the WDA, and Figure 12(b) shows that the largest-amplitude fluctuations occurred just after the arrival of the WDA.

Support for our interpretation of the data in Figure 12(b) in terms of large-amplitude waves at the top of the undercurrent is provided by the dashed line drawn in this diagram between 1240 and 1325 which shows a streamline approaching the front of the storm at 1600 m and then rising to 2500 m before plunging down to near 1000 m. This streamline was inferred from the shape of the uppermost layer of negative wind shear as measured by the nearby Chilbolton Doppler radar (shown later in Figure 16) and was converted to the temporal plot according to the system velocity. The location of the cusped waves shown by the dashed radar-derived line is consistent with the waves shown by the alternating greens and yellow colours in the wind-profiler data, given the uncertainty in the time–space adjustment required to superimpose the radar-derived line on the wind-profiler time series.

6. Structure of the undercurrent wave as measured by the aircraft

The Dornier aircraft flew a level track at 1540 m above mean sea level within the undercurrent ahead of MCS C between 1202 and 1226 as the storm approached Chilbolton. In Figure 13 the location of this track has been adjusted relative to the position of the storm at 1215 assuming a system velocity at this earlier time of 15 m s^{-1} from the south-west. The aircraft track is colour-coded in Figures 13

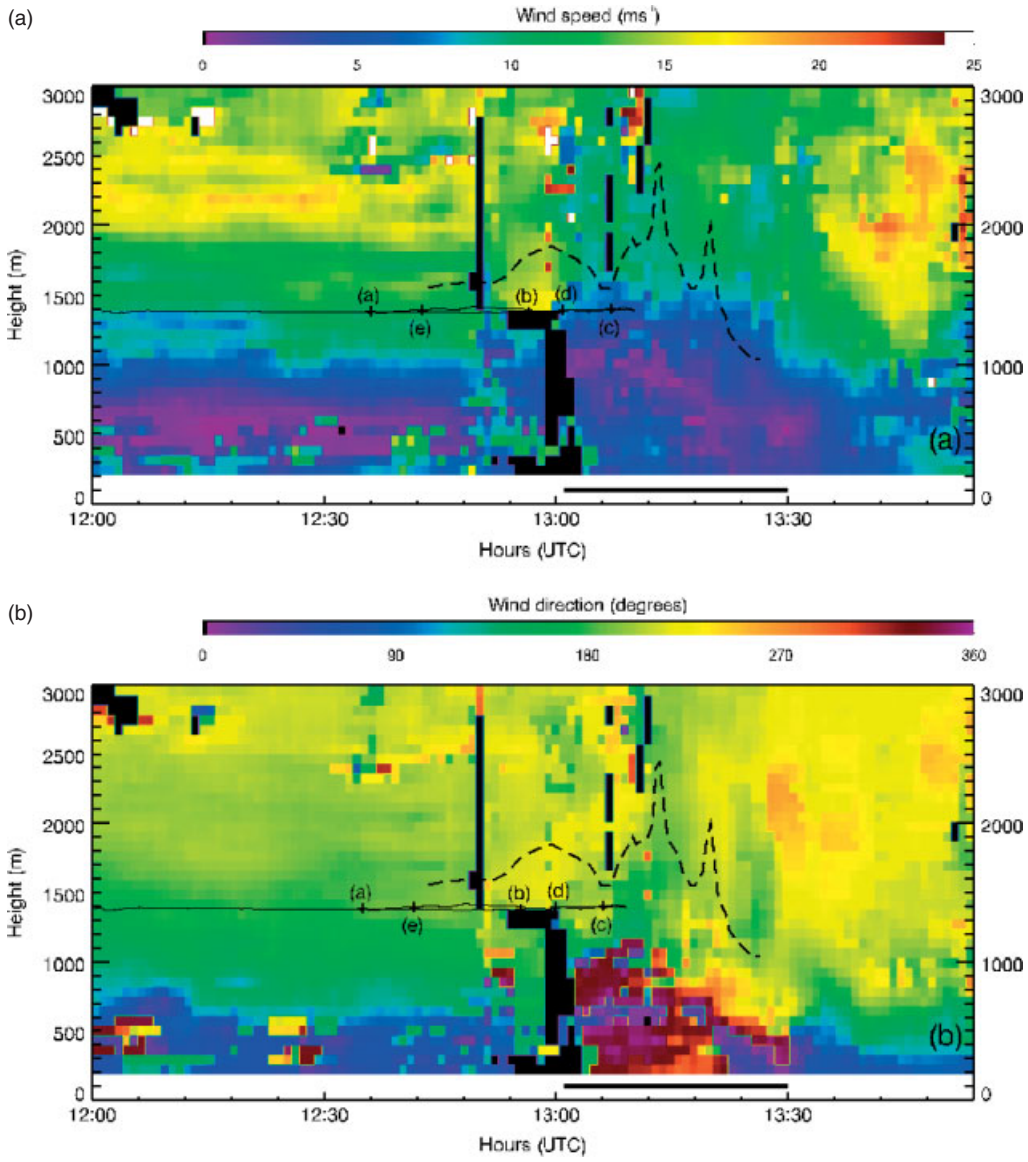

Figure 12. Time series of profiles of (a) wind speed and (b) wind direction, from the wind profiler at Linkenholt (approximately 20 km north of Chilbolton, see map in Figure 2). Heights are above ground level. Erroneous data values are masked black. The horizontal black lines below the plots show the time–space adjusted near-surface wind-direction anomaly (WDA) from Faccombe (see map in Figure 2), where the wind direction was west of north. The dashed black line shows the time–space adjusted line of constant shear from the Chilbolton radar that is plotted in Figure 16 and is believed to be representative of a streamline. The thin black line labelled (a) to (e) is the location of the time–space adjusted aircraft leg shown in Figure 13.

and 14, with the time series depicted in Figure 14 shown as equivalent spatial plots resolved along the 232° azimuth from Chilbolton (again assuming a 15 m s^{-1} system velocity).

Most of the aircraft flight was ahead of the storm's rain area; only the portion of the track coloured cyan was in rain (as detected by the videos from the aircraft cockpit). It entered the rain at 1217 and then, at 1218, due to safety considerations, it turned around and exited the rain area at 1220. Figure 13 shows that the fit between the rain detected by the aircraft and the radar network is good, despite the 2 to 5-minute time difference between the two datasets. Similarly, at the transition from red to yellow data points, Figure 14 shows the downwelling shortwave radiation starting to decrease rapidly, and Figure 13 shows that this gives a good agreement with the extent of the cirrus anvil shown by the Meteosat imagery. In the discussion below we show that the transitions from yellow to green and blue to purple data points (labelled (a) and (e) in Figure 13) correspond to where the aircraft entered and exited the leading portion of the wave in the undercurrent.

The first aircraft spiral profile at 1200 (dashed line in Figure 15) was 40 km ahead of the rain and the second spiral profile at 1230 (solid line in Figure 15) was 20 km ahead of the rain. (Comparison with a radiosonde launched from Chilbolton at 1200 suggests that the absolute values of theta-w measured by the aircraft were about 1°C higher than the radiosonde; however, it is only the relative values that we shall be using in this section.) The aircraft profiles are in good agreement with one another, albeit with a height shift of about 200 m between the main features, consistent with the region between 40 and 20 km ahead of the rain being where the undercurrent was descending and had not yet commenced its ascent into the wave. The aircraft profiles show a maximum in theta-w between 1000 and 1200 m (labelled 'A') and a minimum between 1300 and 1500 m (labelled 'B'). These correspond, respectively, to flows identified by Browning *et al.* (2010) for an earlier

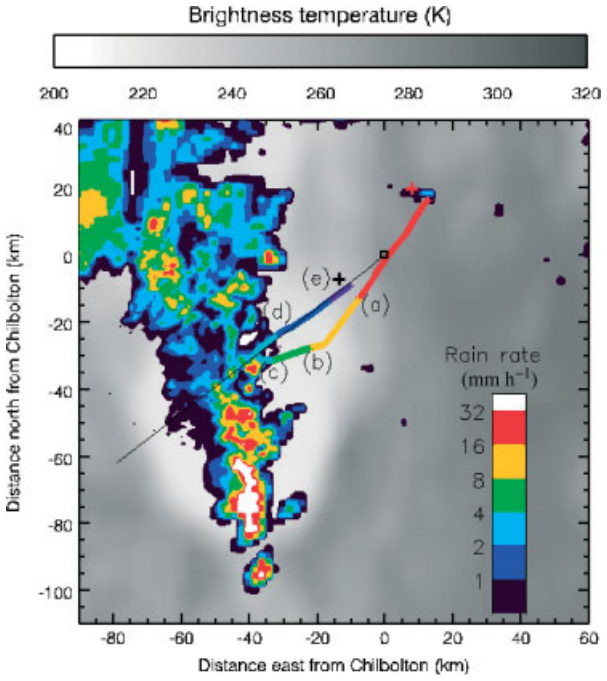

Figure 13. Rain-rates retrieved from the network radars (coloured) and 11 μm brightness temperatures from Meteosat (grey-scaled) at 1215 UTC. The coloured lines show the system-relative aircraft track, with colours and code letters denoting significant parameter changes shown in Figure 14 and described in the text. The solid black line shows the 232° azimuth of the RHI scan shown in Figure 16 (this is the nearest available RHI to the aircraft track). The square shows the location of the Chilbolton radar. The red and black crosses show the mean locations of the aircraft profiles (shown in Figure 14) taken at 1155 to 1203 UTC and 1227 to 1238 UTC, respectively.

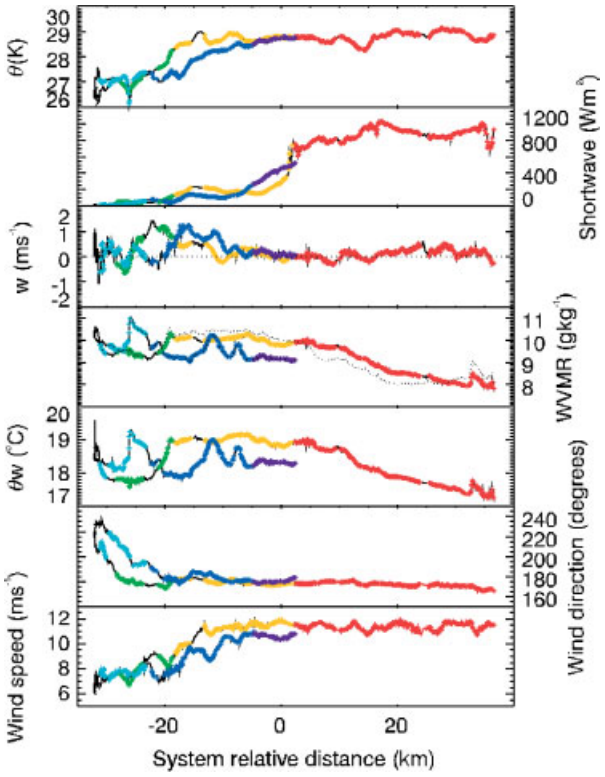

Figure 14. Observations of potential temperature ('θ'), downwelling solar radiation ('shortwave'), vertical wind ('w'), wet-bulb potential temperature (θ_w), and horizontal wind direction and speed from the level leg of the Dornier aircraft (between 1202 to 1226 UTC). Data from straight and level legs are shown in colour (otherwise in black). For WVMR, the dotted black line shows results from the HumiCap, and the coloured symbols show the best combination of this with the Lyman-Alpha for times when both were available (discussed in text). Data are from the outward and return tracks shown in Figure 13, and are plotted against distance along 232° from Chilbolton relative to the system at 1233 (the direction and time of the RHI shown in Figure 16, with negative values towards the south-west).

time as Flows 2 and 3. The double maximum in theta-w around 2000 and 2500 m (labelled 'C' and 'D') appears to correspond to what was analysed in the earlier data as Flow 4.

The coloured points in Figure 15 show the wide range of theta-w values from the aircraft's horizontal leg; these are partly influenced by horizontal variability in the properties of the air flow, but are mainly due to the differing vertical displacements experienced by different portions of the undercurrent flow encountered. We now return to a more detailed analysis of Figure 14 in order to obtain a semi-quantitative estimate of these vertical displacements.

The green data points show two distinct periods of fairly rapid changes (at −18 to −23 km and −23 to −28 km in Figure 14). The first period shows upward vertical winds, theta decreasing and theta-w decreasing. The second period shows varying, but predominantly downward, vertical winds, decreasing values of theta, and more constant values of theta-w and WVMR. The first period (with decreasing theta-w) is thermodynamically consistent with the ascent of drier air, i.e. the aircraft encounters the transition region between layers 'C' and 'B'. Over the 4 km extent of this first part of the green data, using theta or theta-w, we infer that the air observed has ascended by 170 m, corresponding to an ascent rate of approximately 0.5 m s^{-1}. The direct aircraft measurements indicate even stronger ascent, by a factor of two. We conclude that at this time the aircraft was within the ascending portion of the wave in the undercurrent, and this is later shown to be consistent with the radar data (Figure 16).

The second part of the green data (with more constant theta-w and increasing WVMR) and the cyan data

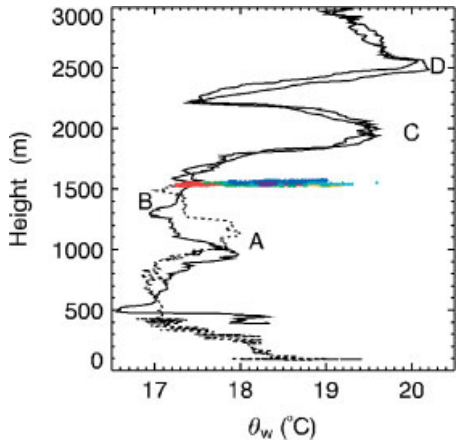

Figure 15. Values of theta-w derived from aircraft profiles and legs. The solid black line shows the later profile (1227 to 1238) and the dashed line the earlier profile (1155 to 1203). Coloured points are from the leg shown in Figures 13 and 14.

points from within the rain are largely thermodynamically consistent with evaporative moistening of the previously observed green points from within the wave (not shown). Within the rain (cyan data) there were periods of increased WVMR (and theta-w) that were associated with either upward or downward vertical velocities (Figure 14). Within the leading part of the rain area, the winds and the properties

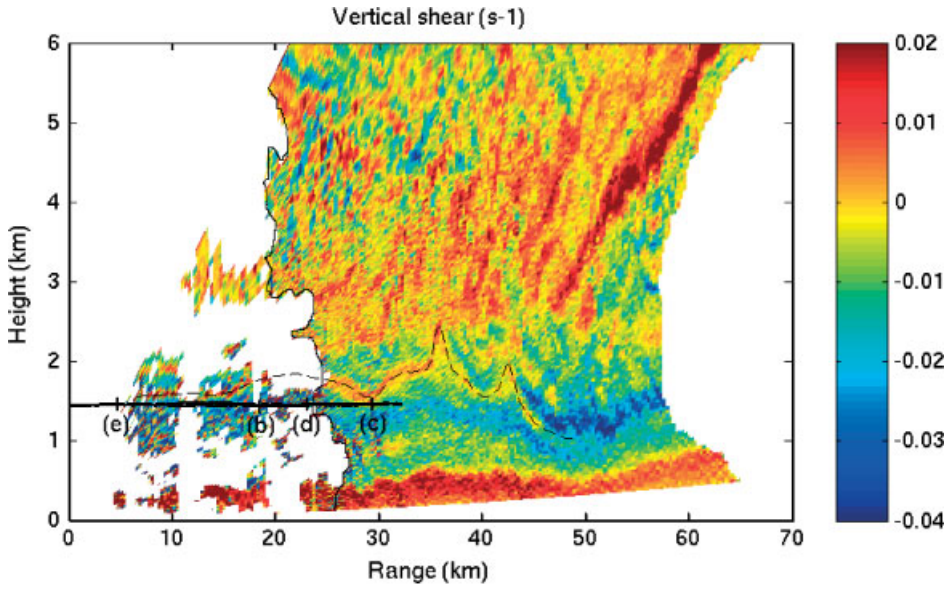

Figure 16. Wind shear (s^{-1}) from the 232° RHI from Chilbolton at 1233 (other fields are shown in Figs. 10 and 11 of Browning *et al.*, 2010). The bold horizontal black line shows the system-relative aircraft track, with the same code letters as shown in Figure 13. The solid black line shows the leading edge of precipitation echo and the dashed black line highlights the single layer that is superimposed on the wind-profiler data in Figure 12. Range is positive towards the southwest, with the storm moving from right to left.

of the air fluctuated rapidly, with a horizontal wavelength of about 6 km. Thus the local increases in WVMR of order 1 g kg^{-1} are most likely to have been due to evaporation within rain shafts separated by 6 km. This is supported by the accompanying drops in theta to minima of about 26°C.

Figures 14 and 15 show that the return flight tended to retrace the values obtained during the outward leg, albeit with somewhat lower and more fluctuating values of WVMR and theta-w. The strong upward motion detected between 5 and 12 km ahead of the rain area was associated with increases in WVMR, theta and theta-w, consistent with the aircraft flying back through the rising part of the undercurrent wave. The decreasing theta-w and WVMR values in the later blue and purple data are consistent with the aircraft retracing its route through a region of subsidence of about 0.1 m s^{-1}, as was also seen on the approaching leg (the red and yellow data).

The changes in wind speed and direction measured by the aircraft while it was within the wave were also notable (Figure 14). The decrease in wind speed, from approximately 11 to 7 m s^{-1} observed by the aircraft is broadly consistent with the wind profiler data in Figure 12(a), although there is a 15 min (15 km) discrepancy in the timing (position) of the change owing to the difficulty in transposing the aircraft track onto the wind-profiler record obtained from roughly 30 km to the north of the aircraft at this time. After being consistently from 180°, the wind veered steadily in the rain, reaching 235° when the pilot decided to turn back. This would be consistent with the aircraft flying from a green region of the wind-profiler record in Figure 12(b) into one of the yellow regions that extended downwards in this record; however, relating the timing (position) of this change in the two sets of measurements is again problematic because of the separation of the measurements in time and space.

Figure 16 shows Doppler shear from the 1233 RHI along the 232° azimuth (shown in Figure 13). (This same scan was used in Figs. 10 and 11 of Browning *et al.*, 2010). The dashed line in Figure 16 (also shown in Figure 12) highlights the mid-point of the (orange/yellow) layer of minimal wind-shear and undulates with a wavelength of 4 to 8 km within the precipitation area. This line is also extended into the region of clear-air echo at ranges less than 24 km; although the wind-shear record is very noisy within the weak clear-air echo, coherent layers can be discerned, except within the 5 kilometres ahead of the rain (i.e. left of the solid line) where the dashed line has been derived by interpolation. The direction of the undercurrent flow is from left to right in Figure 16 and so the region between 11 and 5 km ahead of the rain was evidently a region of ascent associated with the undercurrent wave. This ties in well with the aircraft measurements (the system-relative locations of which are shown in Figure 16), with the aircraft experiencing air rising by between 170 to 340 m in 4 km, ahead of the rain. Within the rain area, beyond the point where the aircraft turned round, Figure 16 shows that the amplitude of the wave was much greater and, indeed, became sharply cusped.

In summary, due to large-scale variations in thermodynamic properties of the air, compounded by the failure of the Lyman-Alpha water vapour sensor, the aircraft data could not be used to determine the precise level of origin and extent of evaporation of the air observed in the wave. However, the *in situ* aircraft data support inferences made from profilers and radar Doppler winds, in that at an altitude of 1540 m and 10 km ahead of the rain it shows sharp ascent of 0.5 to 1.0 m s^{-1}. The thermodynamic data from the aircraft also support the evidence from the Chilbolton radar of weak (~0.1 m s^{-1}) subsidence ahead of this ascent. Within the rain, evaporation of precipitation was detectable, but did not appear to have moistened the air at 1540 m by more than 1 g kg^{-1}.

7. The effects of cloud shadowing and the undercurrent wave as it tracked through the surface network

In this section we show that the surface signatures of the MCS and associated wave, already shown in Figures 4 and 5, were coherent throughout the period that the MCS was

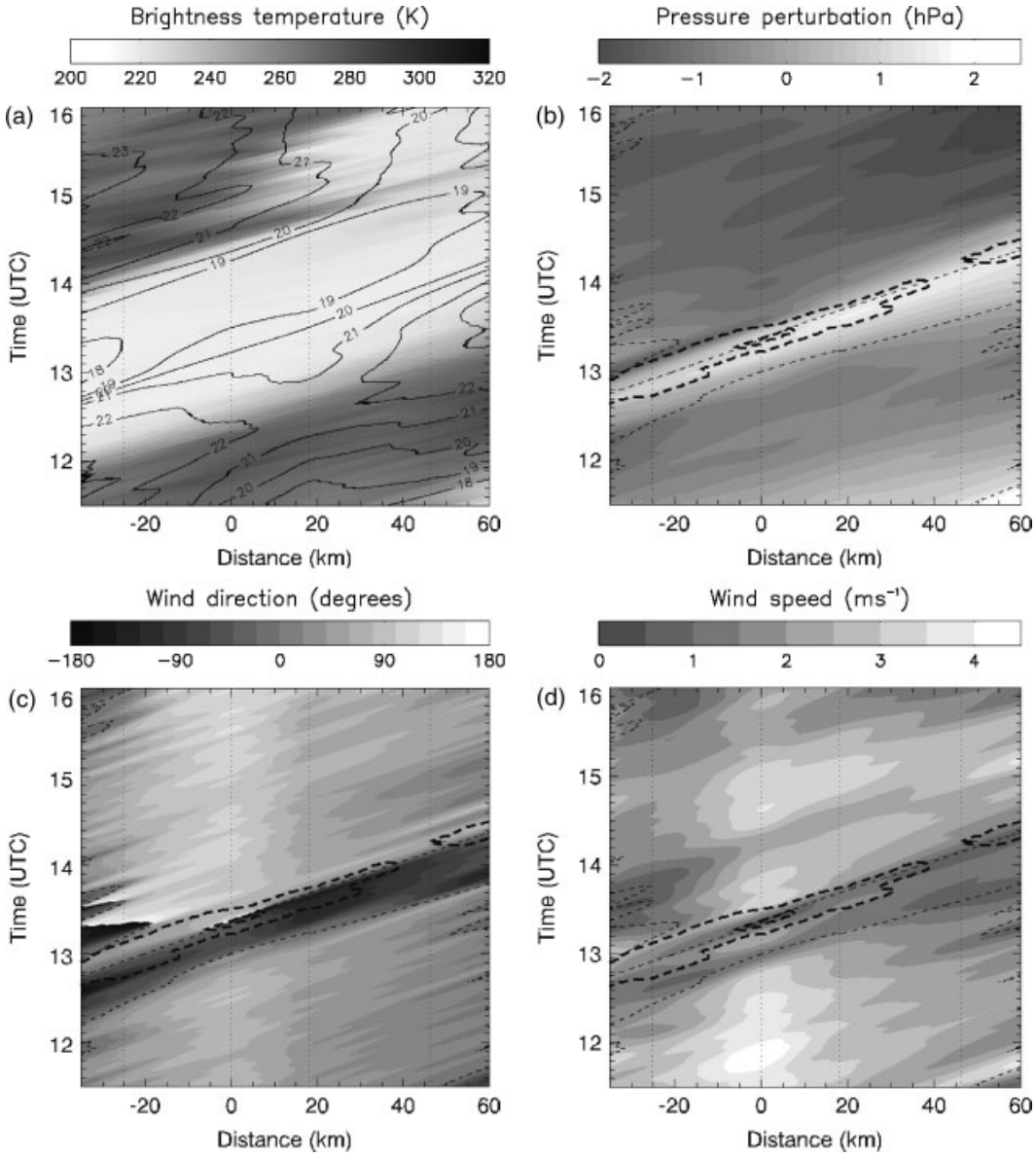

Figure 17. Hovmüller plots of data from AWS sites 22, 26 (Chilbolton, see Figure 4), 14 and 27, showing (a) 2 m air temperatures (contoured with 1°C contour spacings) and 11 μm Meteosat brightness temperatures (grey-scaled), (b) AWS pressure perturbations (grey-scaled), (c) AWS wind directions (grey-scaled), and (d) AWS wind speeds (grey-scaled). Data have been interpolated obliquely using the speed derived from the uninterpolated data, and a parallax correction was applied to the Meteosat data in (a). In (b), (c) and (d) the thick black dashed line in each plot shows a rain-rate (from network rain-radars) of 8 mm/hour and the thin black dashed lines show single contours of northerly wind direction; this main transition from winds east-of-north to winds west-of-north, just ahead of the pressure maximum, delineates what is referred to as the 'wind direction anomaly', or WDA.

crossing the CSIP observational network. We also show that a significant evaporatively driven cold-pool outflow was never observed, but first we show that the surface-temperature effects were largely a result of reduced insolation from the MCS cirrus anvil.

7.1. Effects at the surface of cloud shadowing and rain evaporation

Figure 17(a) is a Hovmüller plot of surface temperature derived from four AWS sites aligned along the storm's direction of travel (225–045°). The Hovmüller plot shows the region of 3 to 4°C fall in temperature progressing steadily at about 60 km/h across the network of stations, and the data in the Hovmüller plot have been interpolated along axes corresponding to this speed. The onset of the temperature fall is seen to have coincided throughout with the passage overhead of the leading edge of the anvil cloud shield as given by the Meteosat infra-red data. Similarly the surface temperature can be seen to have recovered after the passage of the anvil cloud, although the recovery was delayed, especially at distances beyond 20 km, by further high cloud developing behind the main anvil. This, together with the close correspondence between insolation, surface fluxes and 2 m temperatures in Figure 4, suggests that the overall decrease in surface temperature, and probably also the decrease in WVMR, during the passage of the MCS were due, in large measure, to a reduction in surface fluxes accompanying the reduced insolation. The overall increase in relative humidity as the WVMR decreased (shown in Figure 4) was largely a consequence of the concomitant decrease in temperature.

To test the hypothesis that the observed changes in surface temperature and humidity could have been caused mainly by

the observed changes in surface flux due to cloud shading, we have run version 2.3 of the Met Office Large Eddy Model (LEM) (Gray *et al.*, 2001) initialized with the 1200 radiosonde sounding from Chilbolton. A domain of 5 km by 5 km was used with a horizontal grid-spacing of 50 m. The vertical grid was stretched, with the first model level at 2 m, and a vertical spacing of 50 m at a height of 500 m, reaching 3000 m at a height of 20 km. Periodic lateral boundary conditions were used, with an artificial damping layer above 15 km to avoid reflection off the rigid lid of the model.

The LEM was forced with observed surface fluxes, which were available every 30 min (Figure 4). In order to increase the time-resolution of the forcing fluxes, 10-second sensible and latent heat fluxes were derived from the 10-second observations of downwelling solar flux, using the observed correlations between solar and surface fluxes (0.81 and 0.75 for half-hourly sensible and latent fluxes, respectively). The correlation is not expected to be as large for fluxes on shorter time-scales, but this method allows an estimate of the surface fluxes with a better time-resolution of the effects of the cirrus shading. There are also uncertainties in the observed half-hourly fluxes themselves, especially where the sensible heat flux becomes negative, but using these fluxes to force the LEM allows us to test whether the observed changes in 2 m temperature and humidity are consistent with the observed flux changes, or whether other processes must be important. Figure 18(a) shows the resulting trend in 2 m temperature for the observed (dashed line) and estimated (dash-dotted line) fluxes. For comparison, the solid line shows the observed 2 m temperature as measured by the Chilbolton AWS. Allowing for model spin-up, the model reproduces the observed cooling and rewarming to within 1°C. The decrease in 2 m temperatures while surface sensible heat fluxes are positive is caused by the decrease in the strength of the surface superadiabatic layer (see also Marsham *et al.*, 2007a, 2007b).

Figure 18(b) shows that allowing for the model spin-up before about 1245, the observed trend in WVMR is broadly reproduced by the model, except for the rapid increases in WVMR at 1300 and 1325. These increases may have been due to the effects of evaporation of hydrometeors, which was not represented in the model. The increase at 1325 certainly corresponded to the period of heavy rain measured at Chilbolton (grey lines in Figure 18). Moreover, although the earlier increase in WVMR, at 1300, did not coincide with heavy rain at Chilbolton itself, Figure 3(b) shows that a separate cell of heavy rain passed within 5 km to the north-west of Chilbolton at this time. Thus two episodes of evaporation seem to have been detected, at 1300 and 1325, but they were minor events, creating increases in WVMR of less than 1 and 0.5 g kg^{-1}, respectively (Figure 18(b)). Corresponding temperature decreases of about 0.5°C were observed at these times, which were not captured by the LEM (Figure 18(a)). This supports the hypothesis that these short-lived rapid coolings and increases in WVMR were from evaporation.

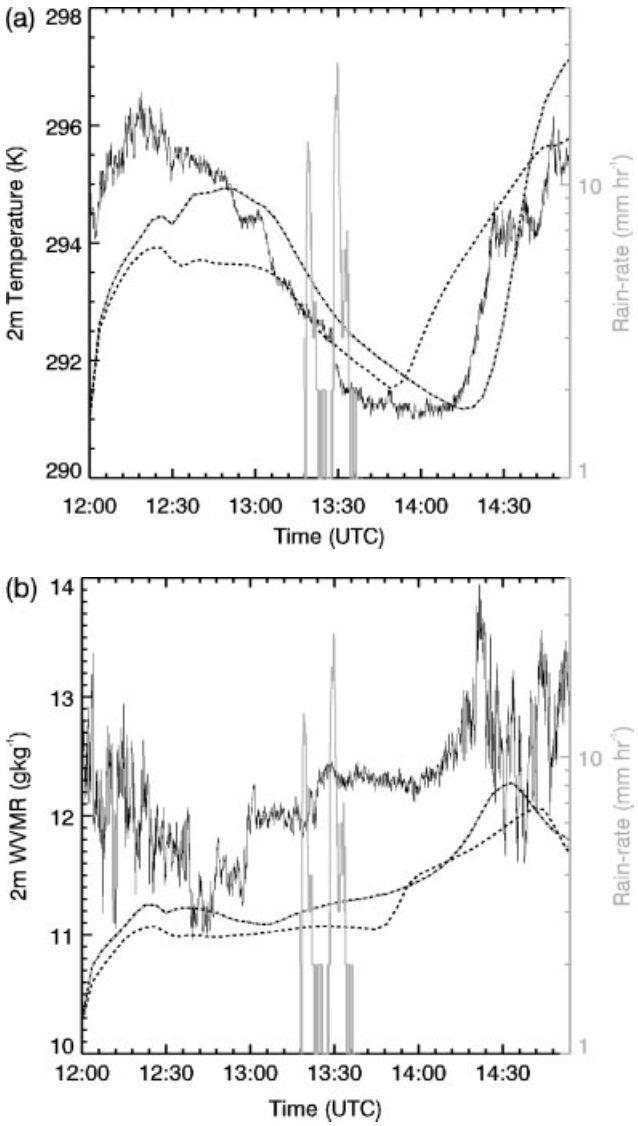

Figure 18. LEM trends in (a) 2 m temperatures and (b) 2 m WVMR, compared with those observed at Chilbolton. The solid black lines show Chilbolton observations, the dashed lines show the LEM forced with observed surface fluxes and the dash-dotted lines show the LEM forced with surface fluxes calculated from the observed solar and surface fluxes (see text for details). The grey lines show observed rainfall.

7.2. *Effects of the undercurrent wave*

The pressure anomaly shown in Figure 17(b) has been calculated from the difference between the instantaneous pressure and the average value of pressure over the entire day. A positive pressure anomaly associated with the MCS, with peak values of about 2.0 hPa, can be seen travelling at about 60 km h^{-1} (as for the temperature anomaly in Figure 17(a)). The data in Figure 17(b) to (d) have been interpolated along axes corresponding to this speed.

Figure 17(b), (c) and (d) show that the surface-pressure and wind anomalies were consistent and rather steady-state features of the MCS, and that they travelled at a velocity similar to that of the storm's rainfall core. The thin dashed contours in each of these figures show a northerly wind direction, i.e. they show the onset and cessation of the WDA that was observed at each of the AWS sites. (We have shown in earlier sections that the WDA extended roughly vertically within the cool undercurrent where the depth of the cool air increased in association with the wave.) The WDA and the maximum in the surface-pressure anomaly were both situated close to the leading edge of the rainfall core, with the WDA marginally leading the pressure anomaly (by 5 to 10 km). Figure 17(d) shows that, at each AWS site, two wind-speed minima were observed, corresponding to the

near-reversal of wind direction at the start and end of the WDA. Between these, a small local maximum in wind-speed was observed, but with slightly greater wind-speeds both ahead and behind the WDA. These relationships between pressure, wind speed and direction, shown over 95 km and 5 hours in Figure 17, are consistent with those shown in x–y space at 1330 in Figure 5. (Not shown in Figure 5 is that all seven AWSs used in that Figure showed wind-speed minima at the start and end of the WDA, consistent with Figure 17(d).)

Finally, Figure 17 shows that throughout the entire domain of the figure, the observed pressure rise was never associated with an abrupt wind-speed increase and rapid cooling, as would have been observed if there had been a significant evaporatively driven cold-pool outflow.

8. Observational synthesis

The observed structures described in sections 3 to 7 are summarized in this section using the idealized depiction in Figure 1. Only the lowest 6 kilometres of the storm are shown here. A broad overview of the storm structure at all, including the higher, levels is shown in Browning *et al.* (2010). Essentially, only two inflows towards the front of the storm are depicted in Figure 1. The lower one (shown green) is the undercurrent air, none of which ascends buoyantly into the main updraught. The upper flow (red) is a simplified portrayal of two inflow layers of high theta-w into the main updraught. The arrows and lettering systems used in Figure 1 are explained below in Table I in the form of an extended key. The main substance of the synthesis is contained in this Table. A limitation of this synthesis is that it is an instantaneous 2-d depiction, i.e. an x–z section where x is along the storm's direction of travel, whereas the observations were obtained at different y locations and over a period of time. The locations of the observations ranged over about 60 km in the y-direction and over a 2-hour period. Although the observations were obtained over a period when the storm system, especially the lower part of the undercurrent, was fairly two-dimensional and steady state, this is still only an approximation and there is therefore some variation in the structures observed by the different platforms. These variations are reflected in the spread of values given in Table 1.

9. Discussion

9.1. Hydrostatic effect of the wave

In order to estimate the hydrostatic pressure anomaly at the surface arising from the lifting of undercurrent air by the wave, we have plotted two potential temperature profiles in Figure 19. The profile shown by the solid black curve corresponds to that measured by the aircraft largely at 1234 (see caption), at a position about 20 km ahead of the leading edge of the rain. The dashed black curve has been derived by lifting this profile dry adiabatically by different amounts at different levels, based broadly on the maximum vertical excursion of the streamlines within the (green) undercurrent flow in Figure 1. Because of the crudeness of our analysis of the wave morphology, we have made the simplifying approximation that the maximum excursion from the unperturbed level is half of the unperturbed height. The hydrostatic surface-pressure anomaly resulting

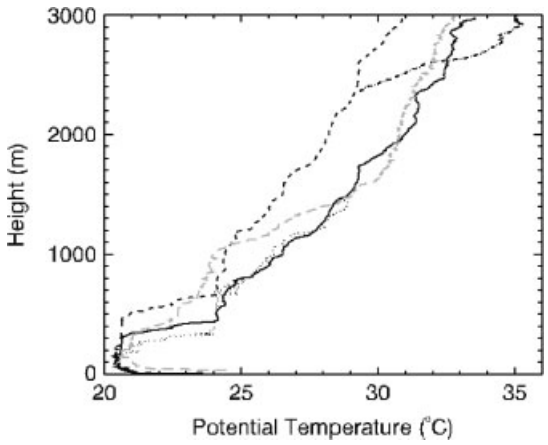

Figure 19. Potential-temperature profile measured from the Dornier 128 (black lines) and the Swanage 1100 radiosonde (long-dashed grey line). For Dornier data above 300 m these were measured between 1232 and 1238 UTC. Below 300 m this has been blended with a profile measured between 1155 and 1203 (dotted line) in order to give a complete profile. The dashed line shows the Dornier profile lifted to 1.5 times its original height without any effects of saturation; the dash-dotted line shows this with saturation effects included (all heights are relative to the height of the airport or Swanage, at 89 and 35 m above mean sea level respectively).

from this lifting is 2.0 hPa (the same value is found using an identical lifting applied to the 1100 Swanage radiosonde, shown by the grey line in Figure 19 and also shown in Fig. 4 of Browning *et al.*, 2010).

The estimated hydrostatic surface-pressure anomaly of 2.0 hPa assumes that all air parcels remained unsaturated during lifting. According to a lidar ceilometer at Chilbolton, the cloud base, although high, lowered to 2300 m just ahead of the rain and so some of the ascent may have been saturated, thereby reducing the temperature anomaly and hence the surface-pressure anomaly. Including saturation when the profile is lifted (dash-dotted line in Figure 19) shows condensation of water above 2250 m, in agreement with the lidar observations. The resultant hydrostatic pressure anomaly is then 1.4 hPa. In addition, a small positive increment in surface pressure will have arisen from cooling of the lower parts of the undercurrent by evaporation of rain. The analysis of Figure 18 suggested that the evaporative cooling at the surface may have been about 0.5°C. If a mean temperature deficit of half this magnitude were applied over the lowest 2 km, this would give a hydrostatic surface-pressure anomaly of +0.5 hPa, giving a total anomaly of around 1.9 hPa, which is comparable to that observed (Figures 5(a) and 17(b)).

We have neglected hydrostatic effects from temperature anomalies above 3000 m (where air densities are lower and hydrostatic effects are smaller) and have taken no account of non-hydrostatic effects. The resulting agreement between the above estimated and observed values suggests that the pressure anomaly observed at the surface can be largely explained by considering the hydrostatic effect of lifting just the undercurrent air. It is also interesting to note that Figures 7, 9, 12 and 16 also suggest the existence of a small local minimum in undercurrent depth under the RIJ, which approximately corresponds to the location of the meso-low identified in the discussion of Figure 4, and also in data from one of the three other AWSs shown in Figure 17(b). However, due to data limitations, we do not pursue the analysis of this feature further.

Table I. Key to the observational synthesis in Figure 1.

The elevated updraught

Updraught inflow: U1-U2-U3 (red arrow)

Layers of air with high theta-w approaching between about 1800 and 3200 m (Figure 15(a), and Browning *et al.*, 2010, Fig. 4)

Main updraught: U4 (red arrow extending upwards above top of diagram)

Consists of both upright and slantwise convection – see Browning *et al.* (2010)

Moderate and heavy precipitation due to main updraught: between R1, R2 and R3, R4 (Figures 4, 5, 7 to 10, 11, 13, 16 and 17)

Cumulus congestus: Above U2 and U3 (Figures 7 to 10)

Extends from 3 km up to 6 km

Located up to 25 km ahead of main updraught (some of the congestus is also ahead of where the underlying undercurrent begins to ascend)

The mid-level downdraught

Rear-inflow jet (slantwise descent): D1-D2 (blue arrow) (Figures 7(b) and 8, and Browning *et al.*, 2010)

Descends above undercurrent to below 1500 m

Some air from it is left behind storm just above the undercurrent

The undercurrent

The undercurrent: S1-S2-S3-S4-S5-S6 (green arrow)

A cool flow below 1800 m approaching front of storm at 10–18 m s^{-1} (Figures 7(b), 8, 10, 12 and 15(a) and Browning *et al.*, 2010). Most of the flow is statically stable except in the convective boundary layer occupying the lowest 200–300 m.

Dry pre-storm descent within undercurrent: S1 to S2 (Figures 10, 11, 14 and 15)

Descent through 100–500 m over 40 km, between 60 and 20 km ahead of rain

Implied average rates of descent: about −0.03 to −0.2 m s^{-1} (the dry descent is not significant above the level of the undercurrent)

Wind direction: between SE'ly and NE'ly (except within wave – see WDA below)

The undercurrent wave and associated features

The overall wave system (including undulations – see below) extends over about 50 km, from S2 to S5.

Ascent at leading edge of undercurrent wave: S2 to S3 (Figures 7 to 10, 11, 12, 14 and 16) – this is quantitatively one of the least consistent features as measured at different times and locations.

Main ascent usually occurs between 0 and 20 km ahead of rain

Amount of ascent varies a lot, from 1000 m to as little as 100 m

Implied average rates of ascent: from about 0.1 to 0.5 m s^{-1}

Some local ascent of about 1 m s^{-1} 10 km ahead of rain

Descent behind undercurrent wave: S4 to S5 (Figures 7(b), 8, 9, 12 and 16)

Consistently large (as much as 1500 m of descent over 20 km)

Implied average rates of descent ∼1 m s^{-1}

The strong descent occurs beneath the nose of the rear-inflow jet

Increase in x-component of wind velocity behind undercurrent wave (Figure 7(b)):

At 250 m it increases from 12 to 26 m s^{-1} (relative to storm) over a distance of 20 km

Wind direction anomaly (WDA): Located within (dashed) envelope W1, W2, W3, W4: (Figures 4 to 6, 12 and 17(c))

Width of WDA at the surface: W1 to W2 = 20 to 30 km

Depth of WDA: W3 to W4 ∼1000 m

Wind direction in the WDA: north-westerly at surface, north to north-westerly aloft

Surface pressure anomaly associated with the wave: (Figures 4, 5 and 17(b))

Maximum 2 hPa

Extent in x-direction 15–40 km

Surface pressure anomaly is collocated with the WDA (W1 to W2), but it lags ∼10 km behind surface-WDA in the less intense northern half of MCS

Its propagation velocity (and that of the MCS as a whole) is 15.5 +/−1 m s^{-1}

Undulations superimposed on overall wave: S3 and S4 (Figures 5, 6, 11, 12 and 16)

Wavelength = 7 km

Amplitude ∼1000 m crest-to-trough above WDA

Sometimes crests are cusped at top of undercurrent

The undulations are associated with double hump in WDA and they appear to be related to a double maximum in surface pressure

The interface between the undercurrent and overlying air from the rear-inflow jet (Figures 7(b) and 9)

Extent of train of Kelvin–Helmholtz-like billows (K1 to K2): about 20 km in x-direction

Amplitude of billows: up to 1 km crest-to-trough

Wavelength of billows: 3 km or less

At a slightly earlier stage in the storm's evolution, Browning *et al.* (2010) identified two layers that had CAPE, which were located at heights of approximately 1.4 and 2.4 km (these are referred to as 'Flow 2' and 'Flow 4' in their Fig. 4). If the lifting discussed above is applied to either the inflow profile measured by the Dornier (Figure 15), or the radiosonde shown in Fig. 4 of Browning *et al.* (2010) for the earlier time of 1100, then in each case the lowest source layer (layer 'A' in Figure 15, or 'Flow 2' in Browning *et al.*, 2010) is just lifted to its level of free convection (not shown). This supports the hypothesis, proposed by Browning *et al.* (2010), that both of the source layers contributed to the upright moist convection, with the wave in the undercurrent providing the lifting required to overcome the convective inhibition (which at 1100 was approximately 70 and 280 J kg^{-1}, respectively, for the upper and lower source layers).

9.2. *The generation of the wave in the undercurrent*

Comparing the low-level flow structure shown in his idealised simulations with the structure shown in Fig. 1 of Klemp *et al.* (1997), Parker (2008) refers to the low-level disturbance in his simulations as a 'bore'. Figures 7 and 8 differ from the schematic of a bore shown in Fig. 1 of Klemp *et al.* (1997); in this case the low-level system-relative flow is towards a stepwise decrease in the undercurrent depth, rather than towards a long-lived stepwise increase. A bore with flow towards the stepwise decrease in flow depth is not possible, as then information (waves) could propagate from the bore towards the shallow flow, leading to a collapse of the bore. Therefore, the disturbance to the low-level undercurrent in this case is not a bore and differs qualitatively from the simulations of Parker (2008).

The variations in the depth of the underlying layer can be regarded as a response to the pressure fluctuations induced by the convective circulations aloft, and the adaptation of some standard analysis from hydraulic theory (Turner, 1973, pp 64–67) can help to analyse the situation. Consider the case of a shallow, dense fluid of density ρ_2 undercutting a less dense fluid in which the density, ρ_1, is a function of downstream distance, x, and pressure is constant with distance at some upper control height, so that the hydrostatic pressure anomaly just below the interface varies with x according to

$$p'(h) = \rho_1(x)\, g\, (H - h(x)), \tag{1}$$

where H is the control height, $h(x)$ is the depth of the shallow undercutting layer, and g is acceleration due to gravity. Such a two-layer system is similar to the schematic shown in Figure 1, with the green arrow showing the lower layer and the red and blue arrows the upper layer. Making the standard assumptions for shallow, steady flow (Turner, 1973), and assuming that the motion in the deep upper layer is slow enough to make non-hydrostatic pressure anomalies relatively small, we use

$$uh = Q, \tag{2}$$

where Q, the shallow-layer volume-flux, is constant, and $u(x)$ is its speed. We then use the Bernoulli relation just below the level $z = h$, in the form:

$$1/2\, u^2 + gh + p'(h)/\rho_2 = \text{constant}. \tag{3}$$

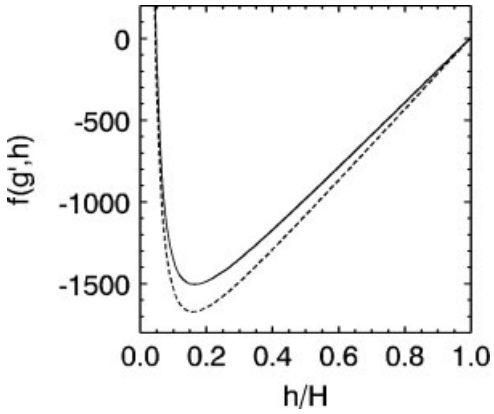

Figure 20. The Bernoulli function, f(g', h), as a function of h/H for a two-layer system (total depth H, lower-layer depth h). The solid line shows this for an increased g' compared with that for the dashed line, i.e. for a decreased density in the upper layer.

Combining these terms we obtain a similar form to that of Turner (1973, p 64):

$$\mathrm{f}(h,\, g') = 1/2\, (Q^2/h^2) - g'\, (H - h) = \text{constant}, \tag{4}$$

independent of x, where $g'(x)$ is the reduced gravity, $g(\rho_2 - \rho_1(x))/\rho_2$.

The function f(h, g') is sketched in Figure 20, with the dashed line showing values for a smaller g', and the solid line showing a larger g'. By inspection of the form of f, or by direct differentiation, we can explore the sensitivity of the shallow layer depth, h, to the hydrostatic pressure imposed by the varying fluid density in the upper layer. The turning-point of f(h) occurs where the Froude number for the shallow later is unity:

$$Fr = u/\sqrt{(g'h)} = 1, \tag{5}$$

so that different behaviour occurs for high (supercritical) and low (subcritical) Fr. When g' increases (i.e. moving from the dashed line to the solid line in Figure 20), with the density of the upper layer falling, keeping f(h) constant requires h to increase if Fr is small, or to decrease if Fr is high (Figure 20). The result can be quantified analytically by writing, for constant f,

$$0 = \mathrm{df} = \partial \mathrm{f}/\partial h\, \mathrm{d}h + \partial \mathrm{f}/\partial g'\, \mathrm{d}g', \tag{6}$$

from which

$$\mathrm{d}h/\mathrm{d}g' = -\partial \mathrm{f}/\partial g'/\partial \mathrm{f}/\partial h = (H - h)/g'\, (1 - Fr^2). \tag{7}$$

Equation 7 shows that if $Fr > 1$, h falls with increasing g', while for $Fr < 1$, h rises with g'. Equation 7 also shows that the maximum amplitude of response occurs when Fr is close to 1, meaning that long waves are stationary relative to the flow speed. Similarly, it can be shown that the surface pressure, p_{surface}, varies with the upper-layer density according to

$$\mathrm{d}p_{\mathrm{surface}}/\mathrm{d}g' = \rho_2\, (H - h)\, Fr^2/(1 - Fr^2), \tag{8}$$

showing that for low Froude number flow, surface pressure increases as the upper-layer density falls (despite the decrease in hydrostatic pressure at a given level in the upper layer).

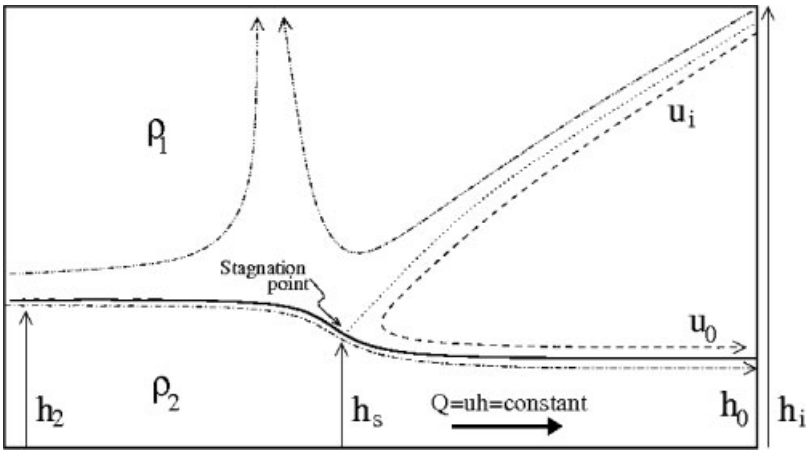

Figure 21. Schematic of the two-layer system used to analyse the impact of the rear-inflow jet on the depth of the undercurrent.

In order to relate this theory to the observations we reduce the complex inflow profiles shown in Figure 19 to two layers. Although the stratifications of all the profiles shown in Figure 19 are similar, this two-layer simplification is more straightforward for the Swanage 1100 radiosonde profile (the grey line) than the aircraft profiles (the black lines), since the Swanage profile has a strong lid at approximately 1.3 km. For the Swanage sounding, we take the approximation of a single lid of $6 \pm 1^{\circ}$C, located at 1.3 ± 0.2 km, separating two neutral layers. This gives observed system-relative velocities of around -15 ± 3 m s^{-1} below the lid and $+5 \pm 3$ m s^{-1} above (see, for example, Figure 7). Using $Fr = u^2/g'h$, with $u = 15$ m s^{-1}, $g' = (6/300)g$ and $h = 1300$ m from the Swanage inflow sounding, gives $Fr = 0.9$ (Fr between 0.4 and 1.8). Similarly, under the rear-inflow jet using $u = 25 \pm 3$ m s^{-1} and $h = 700 \pm 200$ m gives $Fr = 4.5$ (between 2.4 and 9.6), and under the updraught using $u = 12 \pm 4$ m s^{-1} and $h = 2 \pm 0.3$ km gives $Fr = 0.4$ (between 0.1 and 0.9).

These Froude numbers of the observed flow suggest that the observed wave in the undercurrent is consistent with the results of the simple two-layer hydrostatic analysis presented above. The upstream flow conditions show a Froude number which is close to, but just less than, unity. The flow depth increases beneath the convective line, in which the upper-layer buoyancy increases (consistent with h increasing for increasing g', for $Fr < 1$), and the surface pressure increases also. To the rear of the system, in the downdraught zone where upper-layer buoyancy falls, the depth of the flow decreases and the flow appears to go through a smooth transition to a high Froude-number state, analogous to the flow over a hill in classical hydraulic theory (and presumably by upstream control through gravity waves, as discussed by Turner (1973, p 67). This high Froude-number state may be unstable to shear instability on its upper interface, consistent with the features observed between K1 and K2 in Figure 1 (see Table I). This analysis is then consistent with section 9.1, which showed that the observed surface pressure maximum was consistent with the hydrostatic effect of the increased depth of the undercurrent in that location.

The observations suggest that the impacting RIJ constricted the depth of the undercurrent, and it is interesting to consider any possible non-hydrostatic effects resulting from the vertical motions in the RIJ. In order to do this we consider another, similar, two-layer model, which we assume is hydrostatic far upstream and downstream of the system. Considering a streamline starting at the top of the second layer, descending in the rear-inflow and then reversing its flow to exit just above the undercurrent (dashed line in Figure 21), at the top of the upper layer, the Bernoulli function is:

$$\mathrm{B} = 1/2{u_\mathrm{i}}^2 + gh_\mathrm{i} + 0 \tag{9}$$

Considering a streamline descending in the RIJ and terminating at the stagnation point (dotted line in Figure 19(b)) just above the undercurrent, we have:

$$\mathrm{B} = 0 + gh_\mathrm{s} + {p'}_\mathrm{s}/\rho_1, \tag{10}$$

where h_s is the depth of the undercurrent here and ${p'}_\mathrm{s}$ has a non-hydrostatic component. For a streamline just below the top of the undercurrent approaching the system and then passing through a point just under the stagnation point (dash-dotted line in Figure 21) we have:

$$\begin{aligned}\mathrm{B} &= 1/2Q^2/{h_2}^2 + gh_2 + g(h_\mathrm{i} - h_2)\rho_1/\rho_2 \\ &= 1/2Q^2/{h_\mathrm{s}}^2 + gh_\mathrm{s} + {p'}_\mathrm{s}/\rho_2.\end{aligned} \tag{11}$$

Given a constant mass flux Q within the undercurrent, $Q = uh$, and $\rho' = (\rho_2 - \rho_1)/\rho_2$. Noting that by continuity (10) = (9), we have:

$${p'}_\mathrm{s}/\rho_2 + gh_\mathrm{s}\,\rho_1/\rho_2 = 1/2\rho_1/\rho_2{u_\mathrm{i}}^2 + \rho_1/\rho_2\, gh_\mathrm{i}. \tag{12}$$

Equation (11) gives:

$$1/2Q^2/{h_2}^2 + g'h_2 = 1/2Q^2/{h_\mathrm{s}}^2 + g'h_\mathrm{s} + 1/2{u_\mathrm{i}}^2\rho_1/\rho_2. \tag{13}$$

This form is equivalent to the analysis of Turner (1973, p 64) for flow over a small hill, and can be interpreted in the same way (graphically). Alternatively, we can also note that for $Fr < 1$, where the gravitational energy term $g'\,h_\mathrm{s}$ dominates over the kinetic energy, this term dominates the Bernoulli function, in which case, defining $\Delta h_\mathrm{s} = h_2 - h_\mathrm{s}$,

$$g'\Delta h_\mathrm{s} \sim 1/2{u_\mathrm{i}}^2\rho_1/\rho_2. \tag{14}$$

For $\Delta T = 6$ K, giving $g' = 0.2$, and $u_\mathrm{i} = 12$ m s^{-1} (Figure 7), $\Delta h_\mathrm{s} \sim 350$ m. This two-layer analysis therefore suggests that the non-hydrostatic effect as the RIJ impacted

on the undercurrent would have led to a significant constriction of the undercurrent, on a scale comparable with that observed.

Although we cannot add the hydrostatic and non-hydrostatic effects discussed here, due to the nonlinearity of the Bernoulli function, both effects seem to be complementary and consistent with the observed behaviour of the undercurrent. In summary, the above analysis for a two-layer system suggests that for the observed system we expect a deepening of the undercurrent (*Fr* less than, but close to, 1) in response to the moist convection above and then a constriction of the undercurrent below the RIJ, with a smooth transition to a high Froude-number state, with associated turbulence. In this way we expect the wave to be controlled by both the diabatic convective updraughts (perhaps similar to the modelled waves discussed by Schumacher and Johnson (2008) and Schumacher (2009)) and also the diabatic cooling which strengthens the rear-inflow jet (perhaps similar to the modelled waves discussed by Crook and Moncrieff (1988)). Further analysis of the relative contributions of these processes is beyond the scope of this paper (see section 10).

9.3. *Wave speeds in the undercurrent*

The observations show a wave in the undercurrent, which was orientated approximately north–south along the axis of the MCS (Figure 5); the wave was forced by the MCS and propagated with the MCS as it moved northeastwards with the upper-level winds. Section 9.2 shows that this wave could be regarded as a response to the propagating storm over the shallow inflow: the response was seen to be a function of Froude number, itself a balance between natural wave speeds and system-relative advection. As discussed in section 9.2, the form of the observed wave was not that of a bore. It is, however, instructive to compare the speeds of other forms of freely propagating waves with the observed wave in order to enquire whether the wave dynamics of this case could lead to resonance, and amplified response.

Koch *et al.* (1991) gives the speed of a gravity wave propagating on an inversion between two neutral layers, c_{gw}, as:

$$c_{gw} = (g\ \Delta\theta_v\ h_0/\theta_v)^{0.5}, \qquad (15)$$

where h_0 is the inversion height, $\Delta\theta_v$ the virtual potential temperature difference across the inversion and θ_v the mean virtual potential temperature. For the Swanage 1100 sounding (grey line in Figure 19) and considering the largest inversion at 850 hPa (1.3 km), with $\Delta\theta_v = 6$ K, this gives an eastward propagation velocity of 16 m s^{-1}. Considering that the ambient westerly wind below 1.3 km was between −8 and 0 m s^{-1} (Browning *et al.*, 2010, Fig. 4), this is consistent with the observed wave velocity of 11 m s^{-1}. However, Baines (1995, p 58) describes how for a solitary wave on an inversion we expect this velocity to increase by a factor of approximately $(1 + a/2h_0)$, where a is the wave amplitude. Using $a = 650$ m for $h_0 = 1300$ m (section 8), this increases the theoretical wave speed by a factor of 1.5 to 24 m s^{-1} towards the east, which is larger than the observed 11 m s^{-1}, when it is considered that the maximum observed easterly wind in the profile ahead of the MCS was 8 m s^{-1}.

The undercurrent was capped by a stable lid with elevated near-neutral layers above (Figure 19 and Fig. 4 in Browning *et al.*, 2010), which is expected to be favourable for wave-ducting (Lindzen and Tung, 1976; Wang and Lin, 1999). However, the nature and extent of such ducting depends on the vertical wavelength of the wave and requires a more complete investigation than can be included in this paper. The phase velocities for waves travelling in a duct of depth h with constant N, capped by a deep neutral layer ($N = 0$) are given by Nappo (2002, p 100). Figure 19 shows that this two-layer system is also a reasonable idealisation of the profile observed at Swanage, which has $N^2 = 2 \times 10^{-4}$ s^{-2} below 1500 m, and $N^2 = 5 \times 10^{-5}$ s^{-2} above. Numerically solving for a horizontal wavelength of 25 km (Figure 5) gives the phase speed of the fundamental mode as 12.5 m s^{-1}. Again, considering the westerly wind of between −10 and +10 m s^{-1} observed below 1500 m, this is consistent with the observed eastward propagation at 11 m s^{-1}.

These theoretical wave-velocities are similar to the velocity of the MCS and its rear-inflow jet, which themselves moved with the upper-level southwesterly winds. This is consistent with the Froude number of the undercurrent being close to one, so that long waves are stationary relative to the flow speed, which above around 1.5 km was approximately equal to the 11 m s^{-1} eastward velocity of the system. It is interesting to speculate that there may be resonance in the system, where the MCS generates a wave that has a phase speed close to that of the steering-level wind. A similar result was shown in an idealised model by Haertel and Johnson (2000, their Fig. 11); they showed that the surface pressure response in their model increases rapidly as the speed of the cooling imposed approaches the gravity speed associated with its vertical wavelength. For the case considered here, the undercurrent wave was observed to propagate with the MCS rather than independently, the wave always being located just ahead of the rear-inflow jet (see also Browning *et al.*, 2010). A resonance along the lines of that described by Haertel and Johnson (2000), consistent with the $Fr \sim 1$ conditions inferred in the two-layer model of section 9.2, would generate the largest amplitude wave for a wave with a phase-speed close to that of the MCS speed, with the wave (which provided lifting to the source air) also presumably affecting the MCS speed, which was itself constrained by the steering-level winds.

10. Conclusions

On 24 June 2005, during the CSIP field campaign, a series of MCSs affected southern England. The structure of one of these MCSs has been examined in detail by Browning *et al.* (2010), who revealed that it was sourced by elevated layers of high theta-w air located above a stable undercurrent. A wave was shown to have formed in this undercurrent, below the MCS and just ahead of where the rear-inflow jet impacted on and constricted the undercurrent. Using the terminology of Crook and Moncrieff (1988), this wave was a 'gravity wave without stagnation', since the air in the undercurrent was nowhere at rest relative to the system; it was a wave not a bore, since the system-relative flow in the undercurrent was towards a stepwise decrease in the depth of the undercurrent, rather than towards a long-lived stepwise increase.

We have examined the detailed structure of this wave in the present paper using a wide variety of observing systems. Section 8 gives a synthesis of the structure of the wave and so only a few of the details of the structure are repeated below.

Such waves have previously been studied in simulations, but, as far as the authors are aware, this study provides the most complete set of observations of such a wave. Observing the wave in the undercurrent in sufficient detail so as to be able to estimate the induced ascent and descent relied heavily on the 0.28° angular resolution of the 3 GHz wavelength radar at Chilbolton. The novel technique of calculating shear from the observed Doppler velocities (Browning *et al.*, 2010) was also valuable for this purpose. With an angular resolution of 1 degree, more typical for weather radars, much of the small-scale structure would not have been observed. At 50 km range, for example, a vertical resolution of about 300 m was achieved, rather than about 1 km corresponding to a 1 degree beam width.

Key findings are:

(1) The wave moved with the MCS. Surface data show a consistent speed and similar impacts over the entire CSIP network, from 1245 to 1415 UTC over a distance of 90 km. Radar data shown by Browning *et al.* (2010) show that the wave also existed at 1155 and 1430; the wave initially formed and finally dissipated outside of the range of the observations available.

(2) At the surface the wave led to a pressure increase of approximately 2 hPa and lasted about 25 minutes at a given location (corresponding to 25 km). As shown in Figure 1 and Table I, low-level winds were reduced and backed from northeasterly to northwesterly in a region (the 'WDA') just ahead of the pressure anomaly, and the low-level winds in the direction of the system were well correlated with the surface pressure anomaly. The heaviest rain-rates were located at the rear of the pressure anomaly. The surface pressure anomaly can be understood in terms of the hydrostatic pressure perturbation generated by the wave (section 9.1).

(3) There was ascent at the leading edge of the undercurrent wave (100 to 1000 m over 20 km) and even stronger descent behind (approximately 1500 m over 20 km). Undulations were superimposed on the overall wave, with a wavelength of approximately 7 km and a crest-to-trough amplitude of approximately 1000 m. These were sometimes cusped and were associated with a double hump in the WDA and a double maximum in surface pressure.

(4) The lifting generated by the wave, estimated from the synthesis of the observations (and consistent with the observed surface pressure anomaly – point 2 above), was sufficient to raise both of the source layers identified by Browning *et al.* (2010) to their levels of free convection. Therefore, for modelling this case, it is important to represent the extent of the lifting in the wave accurately, if the modelled storms are to be fed from the correct levels. The observed lifting was provided partly by the main wave and partly also by the cusped waves with a wavelength of only 7 km. Resolving the latter is at around the limit of current operational models, which use grid spacings of around 1.5 km (e.g. Lean *et al.*, 2008).

(5) The extended region of cooling observed at the surface (about 4°C) was caused largely by the reduced solar insolation due to the cirrus anvil, rather than evaporation (section 7.1).

(6) Limited evaporative moistening of about 0.5 g kg^{-1} was estimated to have occurred on the basis of observations both at the surface (using an AWS) and in the undercurrent (from aircraft data), but no significant cold-pool outflow was ever observed (sections 6 and 7). The undercurrent was sufficiently cool to prevent the rear-inflow jet from penetrating all the way to the ground, but it is not clear that the evaporative cooling of the undercurrent, by less than 1°C, would have had a significant additional effect in increasing the stability of the undercurrent with respect to the rear-inflow jet.

(7) The observations showed that the uplift in the undercurrent ahead of the MCS was smaller than the descent behind (Table I), which is consistent with the observation that the surface pressure behind the MCS was less than the surface pressure ahead of it (Figure 4). Theoretical analysis of a two-layer system (section 9.2) suggests that the deepening of the undercurrent under the moist convection can be understood as a response of the undercurrent to the moist convection above it, given that the approaching undercurrent had a Froude number close to, but less than 1. The observations suggest that the undercurrent then made a smooth transition to a high Froude number beneath the rear-inflow jet, which is consistent with the turbulence observed between K1 and K2 (Figure 1 and Table I).

(8) The theoretical response of the undercurrent to the moist convection above it in the above two-layer system cannot, however, explain the additional descent observed in the undercurrent under the rear-inflow jet. A theoretical analysis of the impacting rear-inflow jet in the two-layer system suggests that this is expected to have reduced the depth of the undercurrent by an amount of order 300 m, but due to nonlinear effects this cannot simply be added to the descent due to the moist convection. The order of magnitude of this additional descent due to the impacting rear-inflow jet is, however, consistent with the observations. This suggests that the observed distortion of the undercurrent was more a result of the rear-inflow jet, rather than of the moist convection; the undercurrent wave may therefore be expected to be sensitive to the extent of evaporation, sublimation and melting occurring within the rear-inflow jet, but this requires further theoretical or numerical investigations.

(9) In any case, the wave was observed to propagate with the MCS rather than independently of it, and since the estimated phase speed of the wave is comparable with the observed propagation speed of the system (section 9.3), it is interesting to speculate that a resonance may occur between the MCS that is generating the wave and travelling with the upper-level winds, and the wave generated, along the lines of that described by Haertel and Johnson (2000). This would be similar to the wave–CISK mechanisms discussed by Cram *et al.* (1992a, 1992b), where they suggest that in their case-study there was positive feedback between the convection and an internal gravity wave.

Prediction of nocturnal and elevated convection remains a challenging problem for numerical weather prediction (e.g. Davis *et al.*, 2003). The forecast for this occasion from the 1.5 km Unified Model (UM) that was run during CSIP was one of the poorest forecasts from the three-month CSIP

field campaign: the UM showed MCSs, but their locations and propagation exhibited significant errors (not shown). There was only one other day on which an MCS was observed during CSIP. On this day an MCS with a squall-line structure and an extensive cold pool formed close to the Chilbolton radar; this system and its cold pool were remarkably well forecast using the same 1.5 km UM set-up (Clark *et al.*, 2010). It is now important to evaluate the structure of MCSs without extensive cold-pool outflows in NWP models, and the model representation of any associated wave features, such as that described here. Parker (2008) shows that for his idealised case, system velocities depend on whether a cold pool or bore forms at the surface. Whether this occurs in a model, and whether the modelled rear-inflow can penetrate to the surface, is expected to be sensitive to both the stability and humidity of the model profile, and the parametrization of the microphysical processes that both strengthen the rear-inflow and also cool the undercurrent. Furthermore, it is known that the semi-implicit time-stepping used in some operational models for computational reasons can tend to damp gravity waves (Simmons and Temperton, 1997) and this may in some cases limit the model representation of these systems, as well as some surface-based events (e.g. Marsham and Parker, 2006).

Acknowledgements

The original CSIP project and the extended analysis phase leading to the present paper were funded under grants by the Natural Environment Research Council (NERC:NER/O/S/2002 00971 and NE/B505538/1). The authors would like to thank all those involved in the CSIP field campaign. Particular thanks are due to Fay Davies (University of Salford, UK) who ran the radiometer sited at Faccombe, and Norbert Kalthoff (Karlsruhe Institute for Technology, Germany) who ran the surface flux station at Chilbolton. The aircraft data were obtained on board the research aircraft, a Dornier 128 (D-IBUF), of the Technical University of Braunschweig, Germany. Special thanks are due to the crew members: Rolf Hankers, Thomas Feuerle, Mark Bitter and Helmut Schulz for their commitment and cooperation. Rain rates retrieved from the UK network rain radars were provided by the Met Office and data from Meteosat-8 were provided by EUMETSAT. The Chilbolton Observatory is owned by the Science and Technology Facilities Council, funded by NERC and operated by the Chilbolton Group of STFC Rutherford Appleton Laboratory.

References

Andreas EL, Jordan RE, Makshtas AP. 2005. Parameterizing turbulent exchange over sea ice: The Ice Station Weddell results. *Boundary Layer Meteorol.* **114**: 439–460.

Baines PG. 1995. *Topographic effects in stratified flows. Cambridge Monographs on Mechanics*. Cambridge University Press.

Browning KA, Hill FF. 1984. Structure and evolution of a mesoscale convective system near the British Isles. *Q. J. R. Meteorol. Soc.* **110**: 897–913.

Browning KA, Morcrette CJ, Nicol J, Blyth AM, Bennett LJ, Brooks BJ, Marsham JH, Mobbs SD, Parker DJ, Perry F, Clark PA, Ballard SP, Dixon MA, Forbes RM, Lean HW, Li Z, Roberts NM, Corsmeier U, Barthlott C, Deny B, Kalthoff N, Khodayar S, Kohler M, Kottmeier C, Kraut S, Kunz M, Lenfant J, Wieser A, Agnew JL, Bamber D, McGregor J, Beswick KM, Gray MD, Norton E, Ricketts HMA, Russell A, Vaughan G, Webb AR, Bitter M, Feuerle T, Hankers R, Schulz H, Bozier KE, Collier CG, Davies F, Gaffard C, Hewison TJ, Ladd DN, Slack EC, Waight J, Ramatschi M, Wareing DP, Watson RJ. 2007. The Convective Storm Initiation Project. *Bull. Am. Meteorol. Soc.* **88**: 1939–1955.

Browning KA, Marsham JH, Nicol JC, Perry FM, White BA, Blyth AM, Mobbs SD. 2010. Observations of dual slantwise circulations above a cool undercurrent in a mesoscale convective system. *Q. J. R. Meteorol. Soc.* **136**: 354–373.

Buzzi A, Fantini M, Lippolis G. 1991. Quasi-stationary organized convection in the presence of an inversion near the surface: Experiments with a 2-D numerical model. *Meteorol. Atmos. Phys.* **45**: 75–86.

Chapman D, Browning KA. 1997. Radar observations of wind-shear splitting within evolving atmospheric Kelvin–Helmholtz billows. *Q. J. R. Meteorol. Soc.* **123**: 1433–1439.

Clark PA, Browning KA, Morcrette CJ, Blyth AM, Forbes RM, Brooks B, Perry F. 2010. Observations of the evolution of an MCS over southern England. *Q. J. R. Meteorol. Soc.*, submitted.

Coleman TA, Knupp KR. 2009. Factors affecting surface wind speeds in gravity waves and wake lows. *Weather and Forecasting* **24**: 1664–1679.

Colman BR. 1990. Thunderstorms above frontal surfaces in environments without positive CAPE. Part I: A climatology. *Mon. Weather Rev.* **118**: 1103–1122.

Colman BR. 1991. Thunderstorms above frontal surfaces in environments without positive CAPE. 1. A climatology – Reply. *Mon. Weather Rev.* **119**: 2514–2515.

Corsmeier U, Hankers R, Wieser A. 2001. Airborne turbulence measurements in the lower troposphere onboard the research aircraft Dornier 128-6, D-IBUF. *Meteorol. Z.* **10**: 315–329.

Cram JM, Pielke RA, Cotton WR. 1992a. Numerical simulation and analysis of a prefrontal squall line. Part I: Observations and basic simulation results. *J. Atmos. Sci.* **49**: 189–208.

Cram JM, Pielke RA, Cotton WR. 1992b. Numerical simulation and analysis of a prefrontal squall line. Part II: Propagation of the squall line as an internal gravity wave. *J. Atmos. Sci.* **49**: 209–225.

Crook NA, Moncrieff MW. 1988. The effect of large-scale convergence on the generation and maintenance of deep moist convection. *J. Atmos. Sci.* **45**: 3606–3624.

Davis CA, Manning KW, Carbone RE, Trier SB, Tuttle JD. 2003. Coherence of warm-season continental rainfall in numerical weather prediction models. *Mon. Weather Rev.* **131**: 2667–2679.

Dudhia J, Moncrieff MW, So DWK. 1987. The two-dimensional dynamics of West African squall lines. *Q. J. R. Meteorol. Soc.* **113**: 121–146.

Fortune MA, Cotton WR, McAnelly RL. 1992. Frontal wave-like evolution in some mesoscale convective complexes. *Mon. Weather Rev.* **120**: 1279–1300.

Fritsch JM, Forbes GS. 2001. Mesoscale convective systems. Pp 323–357 in *Severe convective storms*, Doswell III CA (ed). *Meteorol. Monographs* No. 50. Amer. Meteorol. Soc.: Boston.

Glickman TS (ed). 2000. *Glossary of meteorology*, 2nd edition. Amer. Meteorol. Soc.: Boston.

Goddard JWF, Eastment JD, Thurai M. 1994. The Chilbolton advanced meteorological radar: A tool for multidisciplinary research. *Electron. Commun. Eng. J.* **6**: 77–86.

Gray MEB, Petch J, Derbyshire SH, Brown AR, Lock AP, Swann HA. 2001. '*Version 2.3 of the Met Office large-eddy model.*' Turbulence and Diffusion Notes 275–277, Met Office, Exeter, UK.

Groenemeijer P, Barthlott C, Behrendt A, Corsmeier U, Handwerker J, Kohler M, Kottmeier C, Mahlke H, Pal S, Radlach M, Trentmann J, Wieser A, Wulfmeyer V. 2009. Observations of kinematics and thermodynamic structure surrounding a convective storm cluster over a low mountain range. *Mon. Weather Rev.* **137**: 585–602.

Haertel PT, Johnson RH. 2000. The linear dynamics of squall line mesohighs and wake lows. *J. Atmos. Sci.* **57**: 93–107.

Kalthoff H, Fiebig-Wittmaack M, Meißner C, Kohler M, Uriarte M, Bischoff-Gauß I, Gonzales E. 2006. The energy balance, evapo-transpiration and nocturnal dew deposition of an arid valley in the Andes. *J. Arid Env.* **65**: 420–443.

Klemp JB, Rotunno R, Skamarock WC. 1997. On the propagation of internal bores. *J. Fluid Mech.* **331**: 81–106.

Knight CA, Miller LJ. 1993. First radar echoes from cumulus clouds. *Bull. Am. Meteorol. Soc.* **74**: 179–188.

Koch SE, Dorian PB, Ferrare R, Melfi SH, Skillman WC, Whiteman D. 1991. Structure of an internal bore and dissipating gravity current as revealed by Raman lidar. *Mon. Weather Rev.* **119**: 857–887.

Lafore J-P, Moncrieff MW. 1989. A numerical investigation of the organization and interaction of the convective and stratiform regions of tropical squall lines. *J. Atmos. Sci.* **46**: 521–544.

Lean HW, Clark PA, Dixon M, Roberts NM, Fitch A, Forbes R, Halliwell C. 2008. Characteristics of high-resolution versions of the

Met Office Unified Model for forecasting convection over the United Kingdom. *Mon. Weather Rev.* **136**: 3408–3424.
Lindzen RS, Tung K-K. 1976. Banded convective activity and ducted gravity waves. *Mon. Weather Rev.* **104**: 1602–1617.
Maddox RA. 1980. Mesoscale convective complexes. *Bull. Am. Meteorol. Soc.* **61**: 1374–1387.
Marsham JH, Parker DJ. 2006. Secondary initiation of multiple bands of cumulonimbus over southern Britain. II: Dynamics of secondary initiation. *Q. J. R. Meteorol. Soc.* **132**: 1053–1072.
Marsham JH, Morcrette CJ, Browning KA, Blyth AM, Parker DJ, Corsmeier U, Kalthoff N, Kohler M. 2007a. Variable cirrus shading during CSIP IOP 5. I: Effects on the initiation of convection. *Q. J. R. Meteorol. Soc.* **133**: 1643–1660.
Marsham JH, Blyth AM, Parker DJ, Beswick K, Browning KA, Corsmeier U, Kalthoff N, Khodayar S, Morcrette CJ, Norton EG. 2007b. Variable cirrus shading during CSIP IOP 5. II: Effects on the convective boundary layer. *Q. J. R. Meteorol. Soc.* **133**: 1661–1675.
Marsham JH, Trier SB, Weckwerth TM, Wilson JW. 2010. Observations of elevated convection initiation leading to a surface-based squall-line during 13 June IHOP_2002. *Mon. Weather Rev.* DOI: 10.1175/2010MWR3422.1.
Nappo CJ. 2002. *An introduction to atmospheric gravity waves. International Geophysics Series*, Volume 85. Academic Press.
Parker MD. 2008. Response of simulated squall lines to low-level cooling. *J. Atmos. Sci.* **65**: 1323–1341.
Rose T, Crewell S, Löhnert U, Simmer C. 2005. A network suitable microwave radiometer for operational monitoring of the cloudy atmosphere. *Atmos. Res.* **75**: 183–200.
Schmidt JM, Cotton WR. 1990. Interactions between upper and lower tropospheric gravity waves on squall line structure and maintenance. *J. Atmos. Sci.* **47**: 1205–1222.
Schumacher RS. 2009. Mechanisms for quasi-stationary behavior in simulated heavy-rain-producing convective systems. *J. Atmos. Sci.* **66**: 1543–1568.
Schumacher RS, Johnson RH. 2008. Mesoscale processes contributing to extreme rainfall in a midlatitude warm-season flash flood. *Mon. Weather Rev.* **136**: 3964–3986.
Simmons AJ, Temperton C. 1997. Stability of a two-time-level semi-implicit integration scheme for gravity wave motion. *Mon. Weather Rev.* **125**: 600–615.
Smull BF, Augustine JA. 1993. Multiscale analysis of a mature mesoscale convective complex. *Mon. Weather Rev.* **121**: 103–132.
Smull BF, Houze Jr RA. 1987. Rear inflow in squall lines with trailing stratiform precipitation. *Mon. Weather Rev.* **115**: 2869–2889.
Trier SB, Parsons DB. 1993. Evolution of the environmental conditions preceding the development of a nocturnal mesoscale convective complex. *Mon. Weather Rev.* **121**: 1078–1098.
Turner JS. 1973. *Buoyancy effects in fluids. Cambridge Monographs on Mechanics and Applied Mathematics*. Cambridge University Press.
Wakimoto RM, Murphey HV, Fovell RG, Lee W-C. 2004. Mantle echoes associated with deep convection: Observations and numerical simulations. *Mon. Weather Rev.* **132**: 1701–1720.
Wang T-A, Lin Y-L. 1999. Wave ducting in a stratified shear flow over a two-dimensional mountain. Part I: General linear criteria. *J. Atmos. Sci.* **56**: 412–436.
Williams E. 1991. Comments on: 'Thunderstorms above frontal surfaces in environments without positive CAPE. Part I: A climatology'. *Mon. Weather Rev.* **119**: 2511–2513.
Wilson JW, Roberts RD. 2006. Summary of convective storm initiation and evolution during IHOP: Observational and modeling perspective. *Mon. Weather Rev.* **134**: 23–47.
Zipser EJ. 1982. Use of a conceptual model of the life-cycle of mesoscale convective systems to improve very-short-range forecasts. Pp 191–204 in *Nowcasting*, Browning KA (ed). Academic Press.

